AN ABSTRACT OF THE THESIS OF

Daniel Ryan Harada for the degree of Master of Science in Applied Physics presented on December 6, 2010.

Title: The Synthesis, Optical, and Transport Properties of $SnZrS_3$

Abstract approved: _____

Janet Tate

Semiconducting materials which can be ambipolarly doped are highly desirable in many electronics applications, including use as solar cell materials. $SnZrS_3$ is being investigated for the possibility of ambipolar doping, with potential applications as a solar cell absorber layer. This dissertation covers the synthesis of $SnZrS_3$ and the related compound Sn_2S_3, as well as measurements of the optical bandgap, Seebeck coefficient, and resistivity of pressed powder pellets for these materials. A reproducible synthesis method by solid state reaction of the elements is developed for $SnZrS_3$. Bandgaps of 1.16-1.21 eV and 1.14-1.15 eV are found for $SnZrS_3$ and Sn_2S_3 respectively. $SnZrS_3$ and Sn_2S_3 are found to be natively p-type, with Seebeck coefficients of +600-700 μV/K and +1000 μV/K. Pressed pellet resistivities of 13 MΩcm for $SnZrS_3$ and 216 kΩcm for Sn_2S_3 are measured. Preliminary doping studies are also carried out.

The Synthesis, Optical, and Transport Properties of $SnZrS_3$

by

Daniel Ryan Harada

A THESIS

submitted to

Oregon State University

in partial fulfillment of
the requirements for the
degree of

Master of Science

Presented December 6, 2010
Commencement June 2011

Master of Science thesis of Daniel Ryan Harada presented on December 6, 2010

APPROVED:

Major Professor, representing Applied Physics

Chair of the Department of Physics

Dean of the Graduate School

I understand that my thesis will become part of the permanent collection of Oregon State University libraries. My signature below authorizes release of my thesis to any reader upon request.

Daniel Ryan Harada, Author

ACKNOWLEDGEMENTS

I would like to thank my research advisor, Janet Tate, for the guidance and support she has given me. She has always been willing to talk and give help whenever I have needed it. I would like to thank Doug Keszler for his help and giving us direction with this project. I am grateful to Annette Richard for mentoring me, and spending vast amounts of her time teaching me all that she knows. Discussions with Andriy Zakutayev have helped guide research, and I want to thank him for his time talking to me. For optical measurements and help interpreting optical data, I would like to thank Josh Russel.

I especially want to thank my wife for her support and encouragement over my grad school career. My parents I thank for their support and interest in all the things I have done.

TABLE OF CONTENTS

TABLE OF CONTENTS (Continued)

LIST OF FIGURES

LIST OF FIGURES (Continued)

THE SYNTHESIS, OPTICAL, AND TRANSPORT PROPERTIES OF $SnZrS_3$

1. INTRODUCTION

The sulfides of Sn and Zr are known to be semiconducting materials, some with transport properties of interest in solar cells. The crystal structure of $SnZrS_3$ has been studied [1], but little is published about its transport properties. There are no reports of values for the bandgap, resistivity, or Seebeck coefficient of $SnZrS_3$. In this dissertation we investigate the synthesis and transport properties of bulk $SnZrS_3$ and the related compound Sn_2S_3.

While there are many studies done on the transport properties of the sulfides of Sn (SnS, SnS_2, and Sn_2S_3) and the sulfides of Zr (ZrS_2, ZrS_3), the range of reported values is wide. Since these materials will be present in some $SnZrS_3$ samples that have not achieved phase purity, we will also measure the transport and optical properties of SnS, SnS_2, ZrS_2, and ZrS_3 as necessary. This will aid us in determining what contributions to measured values are coming from phase impurities, and what can be attributed to $SnZrS_3$ itself.

1.1. The sulfides of Sn and Zr

1.1.1 $SnMS_3$

$SnZrS_3$ crystallizes in the *Pnma* space group [1]. The prototypical compound for this structure is NH_4CdCl_3. Many other chalcogenides of the form $ABCh_3$ occur in this crystal structure, including $SnHfS_3$, Sn_2S_3, and $PbZrS_3$, among others. Figure 1.1 shows

this crystal structure. The Sn has a valence of 2+, and is in a distorted tetrahedron of S atoms. The Zr has a valence of 4+, and is in an octahedron of S atoms. These octahedra form double columns which share two edges, and these columns are linked together by Sn atoms. The unit cell is orthorhombic, with $a = 9.188$ Å, $b = 3.717$ Å, and $c = 13.839$ Å. $SnZrS_3$ has a density of 4.302 g/cm^3. $SnZrS_3$ forms a grey-black powder. Single crystals are red and needle shaped.

Since Sn will also readily take the 4+ valence state, Sn can replace the Zr in $SnZrS_3$ to form the mixed valence compound Sn_2S_3, which can be formally written as $Sn^{II}Sn^{IV}S_3$. This compound also crystallizes in the space group *Pnma* [2]. The unit cell is orthorhombic, with $a = 8.878$ Å, $b = 3.751$ Å, and $c = 14.020$ Å. Sn_2S_3 has a density of 4.754 g/cm^3. Sn_2S_3 single crystals are metallic in appearance [3].

Band structure calculations in Wien2k indicate that $SnZrS_3$ is semiconducting, with an indirect bandgap of approximately 0.8 eV [4]. This band structure is presented in Figure 1.2. It is known that calculations using linear combinations of atomic orbitals (LCAO) will underestimate bandgap values, and so a measured bandgap of higher than 0.8 eV is expected. Sn_2S_3 is predicted to have an indirect bandgap of 0.55 eV. The band structure for $Sn2S_3$ is also shown in Figure 1.2.

The phases of the tin-sulfur system have been studied extensively by Moh, who published an updated Sn-S phase diagram [5]. In his work he attempted the synthesis of Sn_2S_3 at temperatures between 200 and 760 °C. He found that regardless of the temperature, stoichiometric mixtures of the elements Sn and S produced Sn_2S_3 mixed with SnS or SnS_2. He found that at 750 °C the system would reach equilibrium in 48 hours, whereas at 200 °C he sintered the material for over 2300 hours before equilibrium was achieved. Samples that were heated for large periods of time were periodically removed from the oven, ground, and then replaced into the oven. A melting point of 760 °C was found for Sn_2S_3. Sn_2S_3 has a dark grey to slightly metallic color.

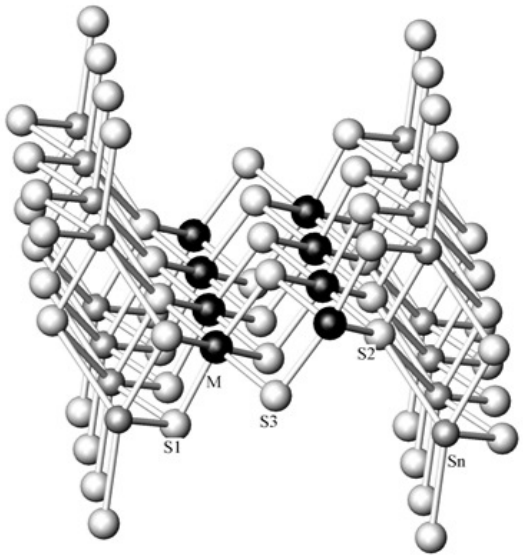

FIGURE 1.1: $SnZrS_3$ crystal structure (M = Zr).

Single crystal measurements of Sn_2S_3 give a room temperature resistivity of 33 kΩ-cm [3]. This paper also reported a bandgap of 0.85 eV from temperature dependent conductivity measurements, and a bandgap of 0.95 eV from optical absorption measurements. The absorption spectra was characteristic of direct forbidden transitions.

1.1.2 Tin Sulfides

In addition to Sn_2S_3, the only known tin sulfides which are stable at low temperatures are SnS and SnS_2 [5]. SnS and SnS_2 are known to tolerate some amount of non-stoichiometry. SnS will remain stoichiometric under Sn rich conditions, but will form $Sn_{1-x}S$ in sulfur rich conditions. SnS_2 will tolerate S deficiencies, forming $Sn_{1+x}S_2$. Sn_2S_3 does not sustain measurable non-stoichiometries at room temperature.

The tin in SnS is in a 2+ valence state. As is the case in SnS, Sn(II) is commonly in a trigonal pyramidal arrangement, with three longer essentially non-bonding contacts which form a distorted octahedron. The longer contacts arise because of the non-bonding electrons on the Sn(II) preventing the ligands from more closely approaching the tin [6]. In

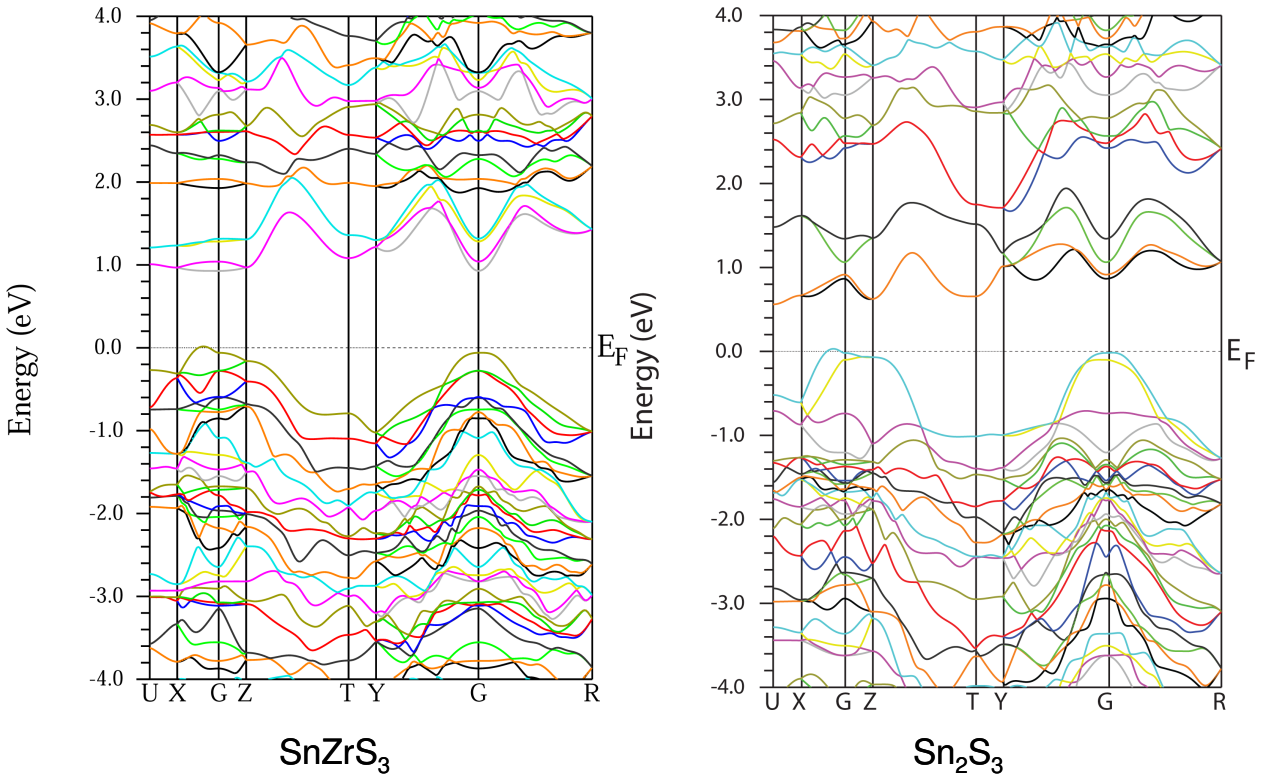

FIGURE 1.2: Band structures of $SnZrS_3$ and Sn_2S_3. Calculated in Wien2k [4].

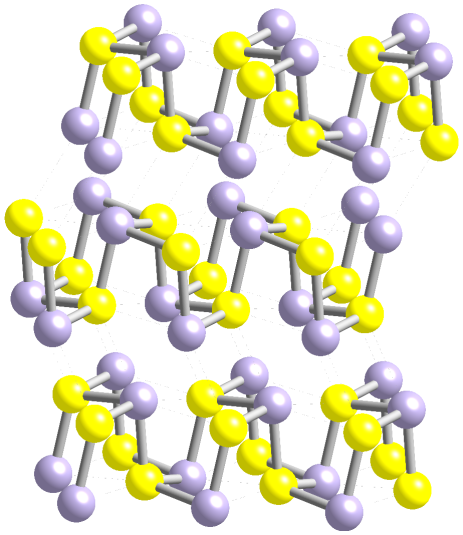

FIGURE 1.3: SnS crystal structure. The Sn atoms are grey, the S atoms are yellow.

SnS the bond lengths to the nearest neighbor S atoms are 2.62 Å, 2.66 Åand 2.66 Å. The next nearest sulfur atom is at a distance of 3.29 Å. The unit cell of SnS is orthorhombic, with $a = 11.18$ Å, $b = 3.982$ Å, and $c = 4.329$ Å. The crystal structure belongs to the *Pnma* space group, and is shown in Figure 1.3. The density of SnS is 5.196 g/cm^3 [7]. It is metallic in appearance.

The optical absorption coefficient for SnS is larger than 10^4 cm^{-1} [8]. Because of the large absorption coefficient and a bandgap in the ideal range for solar cells , SnS is studied as a possible solar cell absorber layer. Other advantages that SnS has are the relatively high abundance of Sn and S compared Ga and In, which are used in CIGS cells, and the lack of toxicity of its constituent elements, which is a problem for cells containing Cd.

SnS thin films have been grown by thermal evaporation [9], chemical deposition [10], electrodeposition [8], as well as other techniques. The optical bandgap for this material has been found to vary significantly depending on deposition technique, deposition conditions, and film thickness. Direct bandgaps in the range of 1.3 to 1.7 eV are reported [9]. Indirect

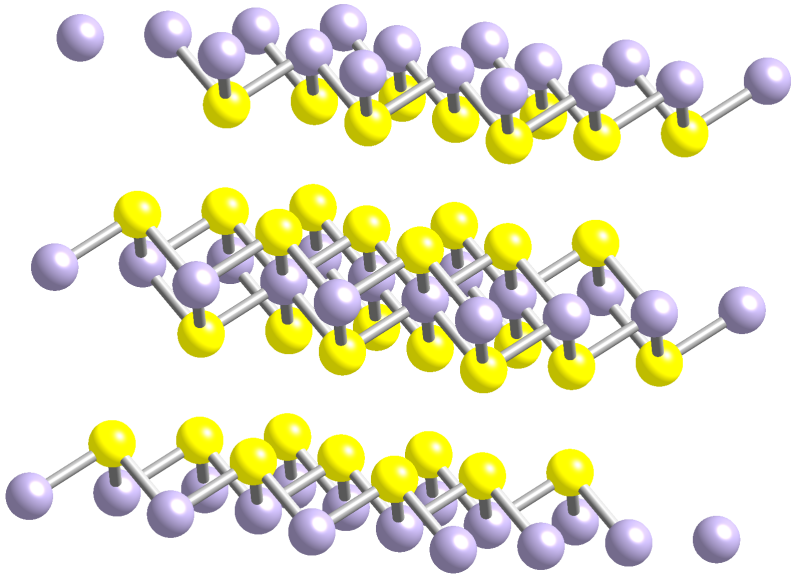

FIGURE 1.4: SnS_2 crystal structure. The Sn atoms are grey, the S atoms are yellow.

bandgaps in the range of 0.9 - 1.1 eV are also reported [11]. LCAO calculations show that SnS has an indirect bandgap [12].

SnS is generally reported as being p-type[9, 13]. The electrical properties are strongly influenced by stoichiometry [8, 13]. Frequently films will also contain small amounts of other Sn-S phases, such as SnS_2 or Sn_2S_3, which will also affect the carrier type and resistivity. Resistivities in the range of 16.8 - 43.1 Ωcm are reported [8].

Moh reports that SnS_2 forms thin plates and twinned crystals that are golden yellow in color [5]. Its unit cell is hexagonal, with $a = 3.647$ Åand $c = 11.811$ Å[14]. The crystal structure belongs to the $P6_3mc$ space group. SnS_2 is a layered structure. The layers are formed by sheets of Sn sandwiched between sheets of S. The crystal structure is shown in Figure 1.4. SnS_2 has a density of 4.463 g/cm^3.

SnS_2 films have been grown using various chemical deposition techniques [15, 16]. Bandgaps are reported in the range of 1.6 - 2.44 eV[16, 17]. Resistivities on the order of 100 Ω-cm have been reported, exhibiting n-type conductivity [16]. As in SnS, stoichiometry

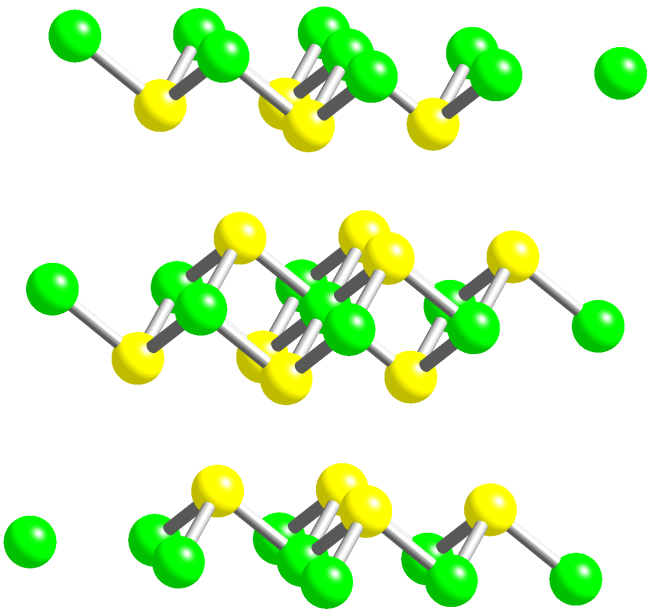

FIGURE 1.5: ZrS_2 crystal structure. The Zr atoms are green, the S atoms are yellow.

in SnS_2 can have an affect on the properties exhibited.

1.1.3 Zirconium Sulfides

ZrS_2 and ZrS_3 are both stable sulfides of Zr, with the Zr atom in the 4+ valence state.

ZrS_2 is an n-type semiconductor reported to have an indirect bandgap of 1.68 eV [18]. Bulk ZrS_2 forms a violet powder [19], and single crystals are reported to be a metallic red color [20]. It belongs to the space group $P3m1$, with a hexagonal unit cell. The lattice parameters are $a = 3.68$ Åand $c = 5.85$ Å. The Zr in is sandwiched between sheets of S atoms. These S-Zr-S layers are then bound to one another by Van der Waals forces [20]. The crystal structure is shown in Figure 1.5.

ZrS_3 belongs to the family of transition metal trichalcogenides TX_3, where T is a transition metal of Group IVB, VB, or VIB, and X is S, Se, or Te. These materials possess a pseudo one-dimensional structure [21]. The T atom will occupy the center of a

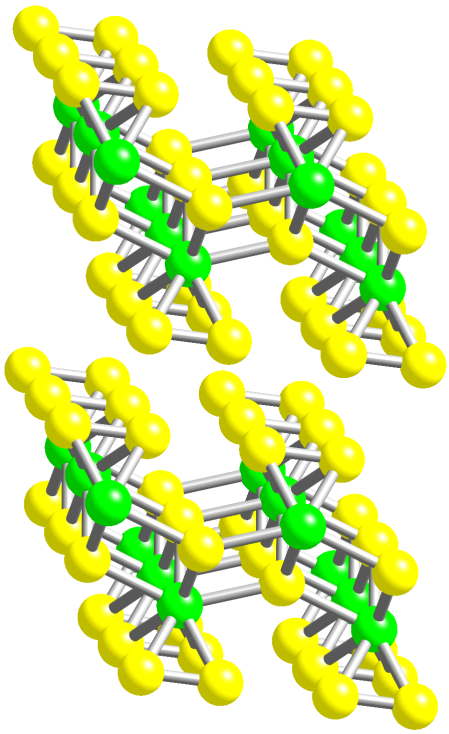

FIGURE 1.6: ZrS_3 crystal structure. The Zr atoms are green, the S atoms are yellow.

trigonal prism with chalcogenide atoms at the corners. Neighboring prisms will share faces, creating an infinite chain along the b-direction of the crystal. The inter-chain bonding tends to be weak, and the inter-chain distances are much large. This gives rise to strongly anisotropic material properties, which has caused interest in this family of materials.

ZrS_3 crystallizes in a monoclinic structure in the $P2_1/m$ space group [22]. The representative compound for this structure is $ZrSe_3$. The lattice parameters are $a = 5.1243$ Å, $b = 3.6244$ Å, and $c = 8.98$ Å, with $\alpha = 97.28°$ [23]. Each Zr is bonded to three S atoms, with two of those S atoms bonding to each other. The crystal structure is shown in Figure 1.6.

Resistivity and Seebeck measurements have been carried out along the b-axis of ZrS_3 single crystals [21]. A room temperature resistivity value of 15 Ωcm is reported. Pressed

pellets of powders have a resistivity which is 10^4 times greater than that of single crystals along the b-axis. The reported Seebeck coefficient is -850 μV/K. Bandgaps in the range of 1.95 eV to 2.56 eV are reported.

2. THEORY AND METHODS

This chapter describes the production and characterization of samples, as well as the theory behind the characterization methods. In the first section production methods will be described, as well as some of the rationale for choosing specific dopants. In the second section X-ray diffraction for phase identification is discussed. The third section is on bandgap determination by diffuse reflectance. The fourth discusses Seebeck measurements as used for determination of majority carrier type. The final section is on resistivity measurements.

2.1. Synthesis and sample preparation

Elemental powders are weighed and then mixed in a mortar and pestle. The powders used for undoped samples are: tin (Sn) (Cerac 99.99%, 200 mesh), zirconium (Zr) (Cerac 99.7%, 325 mesh), and sulfur (S) (Alpha Aesar 99.8%, 325 mesh). This mixture is placed into a fused silica tube which is then evacuated and sealed with an oxygen-hydrogen torch. Typically the tubes are evacuated using a Varian V-70 Turbo vaccuum pump, reaching a pressure of 10^{-6} Torr before being sealed. If the Varian pump is not available, tubes are evacuated on a Welch Duo Seal 1376, which pumps down to 30-50 mTorr. The sealed tubes are then sintered in a Thermolyne 1300 box furnace controlled by a Eurotherm 808 controller. Sinter times are typically 12 hours, and temperatures are detailed in the results section as they vary from material to material. Samples are typically between 0.5 g and 2 g. In samples larger than $\sim$ 3 g, there is the risk of the silica tube popping during sintering due to high vapor pressures inside the tube.

Sintered powders are ground with a mortar and pestle for X-ray diffraction and diffuse reflectance measurements, or they are ground and then pressed into pellets for

transport measurements. The pellets are cold pressed in a ½-inch die to a pressure of 9 metric tons and held there for 10 minutes. Over this time the pressure in the press drops slowly, so periodically the pressure is pressed back up to 9 metric tons. The final density achieved is generally 80% of the theoretical density of the material. The pellets are made from about 1 gram of powder, which produces a 12.7 mm diameter (1/2") pellet 1-2 mm in thickness.

Dopants are introduced into a sample by adding other elemental powders in place of a small amount of the Sn or Zr in a sample prior to sintering. Typically the amount of dopant will not exceed 10 atomic % of the element it is replacing. Dopants used are: niobium (Nb) (Alfa Aesar, 99.8%, 325 mesh), bismuth (Bi) (Strem Chemicals, 99.999%), antimony (Sb) (Alfa Aesar, 99.5%), and indium (In) (Alfa Aesar, 99.9%).

It is important that we are able to predict how the dopant might behave when introduced to the system we wish to modify. There are several criteria that must be examined when choosing a dopant. In a given environment every atomic species will favor certain coordinations, valence states, or some combination of the two. In addition to coordination and valence, the ionic radius of the dopant atom is important. If the ionic radius of the dopant is very different from the element it is replacing, it is likely the crystal lattice will become strained, and the possibility of undesired phases being formed may increase.

Zunger published a paper giving general "doping rules", which give guidelines explaining under what conditions a material is easily dopable n- or p-type [24]. His rules are as follows:

1. n-type doping is facilitated in materials with large electron affinities. Conversely, n-type doping is more easily compensated in materials with small electron affinities.

2. p-type doping is facilitated in materials with small ionization energy. Conversely, p-type doping is more easily compensated in materials with large ionization energy.

3. Cation vacancies compensate n-type dopants. If n-type conductivity is desired, design growth conditions which inhibit cation vacancies.

4. Anion vacancies and cation interstitials will compensate p-type dopants. If p-type conductivity is desired, design growth conditions which inhibit anion vacancies and/or cation interstitials.

5. Dopants which substitute for anions are more soluble under cation rich growth conditions.

6. Dopants substituting for cations are more soluble under anion rich growth conditions.

7. The local chemical bonding energy around the dopant could be enhanced via decorating the dopant by strongly bonding ligands which do not disrupt the host bonds. An example of this is doping N onto the O site of ZnO. The Zn-N bonds are weak, but Al-N bonds are much stronger. If you then replace one Zn with Al for every four N, then the resulting dopant structure is much more stable.

This paper was discovered after the doping work in this thesis was performed, and so these rules will primarily be of use in directing any future doping studies. After it has been proven whether or not the system can be doped n- or p-type, there may also be considerations that affect dopant selection apart from whether or not the dopant will function as intended. These include cost, toxicity, and natural abundance. SnS is being considered as a solar cell absorber material in part because of the abundance and non-toxicity of its components. There have been questions about the extent of the Earth's supply of In [25], for example, so even if In will act as a dopant it may not be the most ideal candidate.

2.2. X-ray diffraction

2.2.1 Theory

XRD on powders is commonly used today in material phase identification [26]. A powder in this sense is any material which contains a large number of small crystals, which are randomly oriented. The basis for XRD is Bragg reflection, where the incident X-rays are reflected off of crystal planes in the sample. Light reflected off of nearby crystal planes will interfere constructively when the path difference between the two beams is a whole number multiple of the incident wavelength. For light with wavelength λ, the incident angles θ_{hkl} which will produce constructive interference from a crystal plane (hkl) a distance d_{hkl} away is found by

$$n\lambda = 2d_{hkl}\sin(\theta_{hkl}) \qquad (2.2..1)$$

where n is the order of the reflection [27].

For a given material, d_{hkl} should be constant from one sample to another for a given (hkl), which means the locations as a function of θ_{hkl} of high intensity reflections should be the same from one sample to another. This gives a method of determining possible phases for a material. Within a given crystal structure the d_{hkl} are generally of similar size from one material to another. This means that the high intensity reflections for materials with a single crystal structure will be in the same general location, but shifted by small angles.

There are two primary methods for measuring diffraction patterns, and angular dispersive method and an energy dispersive method. In the angular dispersive method, a monochromatic X-ray source is used, and the detector is scanned over the desired angle range. In the energy dispersive method, a polychromatic X-ray source is used with the detector held at a constant position. The energies of the reflected X-rays are measured in

addition the intensities at each energy, which effectively scans over λ for a fixed angle.

2.2.2 Experimental

XRD patterns are taken on a Rigaku MiniFlex II benchtop XRD system, which uses Cu Kα radiation. About 0.2 g of prepared powder is packed into an aluminum sample holder. The powder is leveled with a glass slide. For phase identification, scan rates are 3 to 5 degrees per minute. The 2θ increment is 0.02°. Typically the scan is from $2\theta = 15°$ to 50°, but if it is suspected that there is ZrS_3 present, scanning must begin below 10° as the primary ZrS_3 peak is located between 9° and 10°. Recorded patterns are viewed in JADE, and compared with known patterns for the desired phase and possible impurities.

2.3. Diffuse reflectance

2.3.1 Theory

Diffuse reflectance measurements on powders can be used directly to determine the optical bandgap of a material [28]. The onset of optical transitions between the valence band maximum and conduction band minimum is known as the fundamental absorption edge [29]. The energy of the incident photons at the fundamental absorption edge is equal to the bandgap of the material.

In a semiconductor, the diffuse reflectance will decrease linearly with energy at the absorption edge [28]. Examples of diffuse reflectance spectra for several semiconductors are shown in Figure 2.1. The linear regions of these spectra occur at the absorption edge. If there is a clear absorption edge, then the bandgap can be extracted directly from the diffuse reflectance data.

Frequently the onset of absorption will not be clear, as there is not a clear linear region in the reflectivity. In this case we use plots of the absorption coefficient to obtain the bandgap energy. For a semiconductor with a direct bandgap E_g and parabolic energy

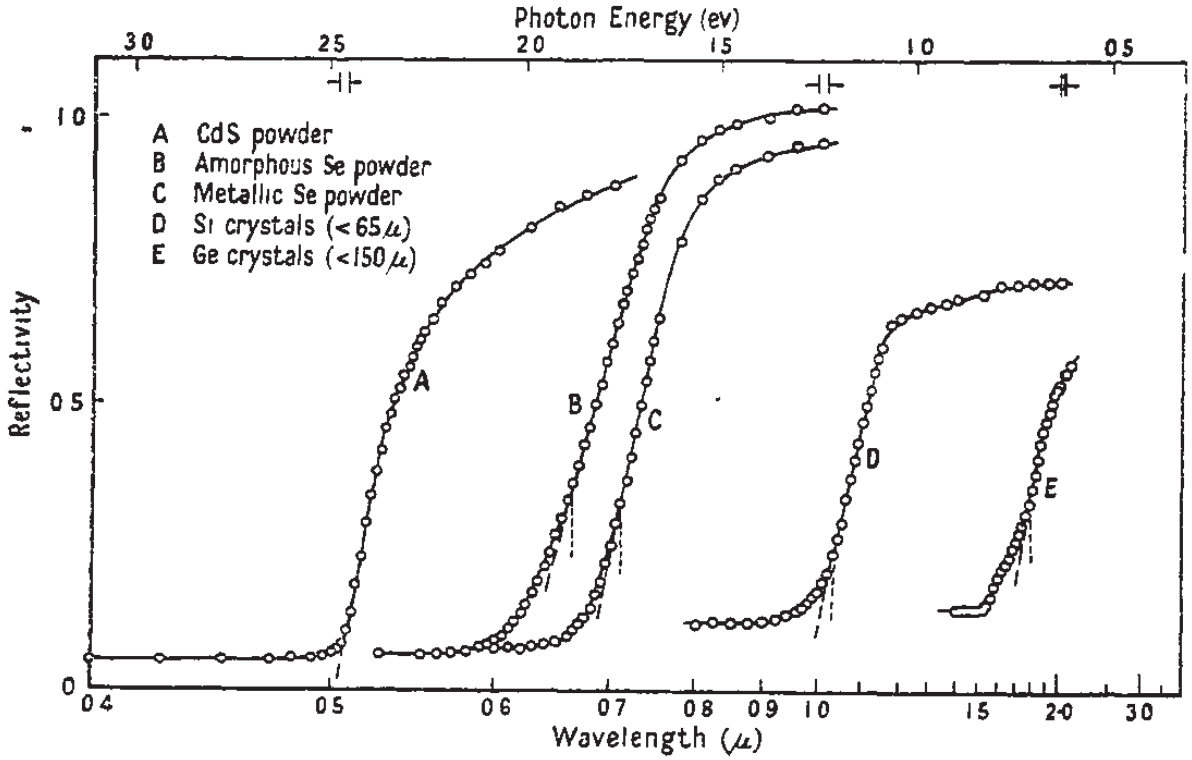

FIGURE 2.1: Diffuse reflectance spectra of several semiconducting powders. The region in which the diffuse reflectance changes linearly with energy indicates the absorption edge for that powder. Image taken from [28].

bands, it can be derived [30, 31] that, near the absorption edge, the absorption coefficient α for direct transitions can be found by

$$\alpha h\nu = A\left(h\nu - E_g\right)^{1/2} \tag{2.3..1}$$

where A is a constant which depends on material properties and $h\nu$ is the energy of the incident photons.

A similar relation for indirect bandgaps can be found. Indirect transitions require the assistance of a phonon, and so its energy must also be accounted for. The relation for indirect bandgaps is

$$\alpha h\nu = A(h\nu \pm E_P - E_g)^2. \tag{2.3..2}$$

where E_P is the energy of the phonon. The + sign is used when a phonon is emitted, and the - sign is used when a phonon is absorbed. The phonon energy will be on the order of k_BT, which at 300 K is approximately 25.9 meV. The bandgaps we will be measuring are on the order of 1 eV, and our resolution is not finer than $\sim$ 0.1 eV, and so we will drop the E_P term from our equations for indirect bandgaps.

Rearranging Equation (2.3..1) gives

$$\left(\frac{\alpha h\nu}{A}\right)^2 = (h\nu - E_g). \tag{2.3..3}$$

When $h\nu$ is above the bandgap energy, a plot of $(\alpha h\nu)^2$ as a function of $h\nu$ should be linear. This line will cross the $h\nu$-axis at the bandgap energy, as when the left hand side of Equation (2.3..3) is zero, $h\nu$ will be equal to the bandgap energy. This gives a method of determining the bandgap energy from absorption data. For indirect bandgaps, the relation is

$$\left(\frac{\alpha h\nu}{A}\right)^{1/2} = (h\nu - E_g), \tag{2.3..4}$$

and one will plot $(\alpha h\nu)^{1/2}$ against $h\nu$ and extrapolate to zero absorption.

Now that we have a method of obtaining the bandgap from absorption data, we must extract this data from the diffuse reflectance spectrum. We are able to obtain information about absorption because not all of the light is reflected at the surface of the sample. There will be some penetration depth, and reflection will occur off of layers that are in the bulk of the sample. As the light passes through the material there will be some probability of absorption rather than reflection or transmission. High absorption will cause the measured reflectivity to drop significantly. At zero absorption we would see a reflectivity of 1, as all of the incident light will eventually reflect out of the sample.

We determine the absorption spectrum through a modified Kubelka-Munk equation [32]. The Kubelka-Munk theory gives a relation between R_∞, the reflectance of an infinitely thick sample, and K/S. K and S are related to the absorption and scattering coefficients, respectively. The Kubelka-Munk equation is

$$K/S = \frac{(1 - R_\infty)^2}{2R_\infty}. \tag{2.3..5}$$

It will be assumed that our samples are sufficiently thick, and R_∞ will be replaced with the measured diffuse reflectance R. It has been shown [33] that $K/S = 2\alpha/s$, where α is the absorption coefficient and s the scattering coefficient. We will assume that s does not vary much over the measured range, and so a plot of K/S will give a good representation of α. We then have a method of converting diffuse reflectance data into absorption data, and can determine the optical bandgap for a material.

2.3.2 Experimental

There are two systems that we use for recording diffuse reflectance spectra. In one system, a diffraction grating is used to select a single wavelength of light. This monochromatic beam is steered with mirrors onto a sample inside an integrating sphere.

The light intensity reflected off the walls of the sphere is recorded by a single detector as we scan through the desired wavelength range. This system will henceforth be referred to as the integrating sphere system.

The second system uses a broadband light source incident on the sample via a fiber optic cable. The reflected signal is then sent via another fiber to a diffraction grating which splits the reflected signal into single wavelength components that are incident on an array of detectors that each measure a specific wavelength region. This system will henceforth be referred to as the fiber optics system. These two systems are diagrammed in Figure 2.2. In both systems a $BaSO_4$ white reference is used.

In the integrating sphere system a tungsten lamp is used as the light source. The light from this lamp is passed through a monochromator, typically with a 1 μm grating. After passing through the monochromator, the light is passed through a filter wheel, which has a set of filters which block light with wavelengths below 300 nm, 600 nm, and 1200 nm. These filters are used to block out higher order light from the diffraction grating. There are also empty slots which provide no filtering.

After passing though the necessary filter, the light is incident upon the sample powder in an integrating sphere. The light is partially reflected off the sample and partially absorbed. The walls of the integrating sphere are diffusely reflective. On the side of the sphere is a photodetector. The spectral intensity is first measured with a $BaSO_4$ reference, then a dark measurement is taken, and then the intensity is measured with the sample in place. The reflectance is the ratio (sample - dark)/(reference - dark). The photodetectors used are a silicon detector which will accurately detect photons with energies above 1.2 eV, and an InGaAs detector which is accurate from 0.6 to 1.3 eV.

For the fiber optics system, there is a separate light source for the UV to visible range (200-1100 nm) and for the near infra-red (NIR) (800-2600nm) range. The UV-vis spectrum is provided by an Ocean Optics Mikropack DH-2000-BAL Deuterium Tungsten

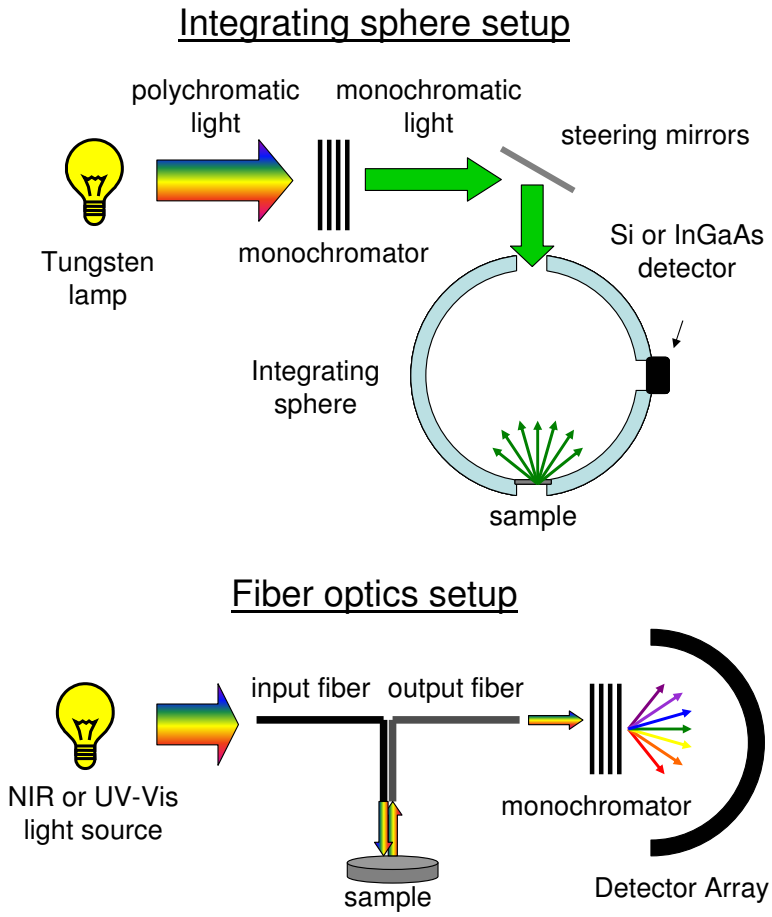

FIGURE 2.2: Integrating sphere and fiber optic setups.

Halogen light source. The NIR spectrum is provided by an Ocean Optics Mikropack HL-2000 Tungsten Halogen light source. The reflectance spectra are measured by an Ocean Optics HR 4000 spectrometer in the UV-vis and by an Ocean Optics NIR256-2.5 spectrometer in the NIR. The NIR measurement used an Ocean Optics QBIF400-VIS/NIR Bifurcated Optical Fiber with a diameter of 400 m. The UV-vis setup utilized an Ocean Optics ZFQ-9803 Bifurcated Optical Fiber with a diameter of 455 m. The other ends of the bifurcated optical fiber were connected to the spectrometer and light source.

The sample is placed approximately 3 mm below the end of the fiber. Measurements are averaged over 1-3 minutes, depending on the intensity of the reflection. By default 100 samples are averaged. The duration of each sample is determined by the number of samples and the integration time. A reference pattern from $BaSO_4$ is first taken, then a dark measurement, then a measurement with the sample in place. The reflectance is found by (sample - dark)/(reference - dark) as before. If both UV-Vis and NIR measurements are desired, the light source must be switched and the measurements repeated.

2.4. Seebeck measurements

2.4.1 Theory

When two different conducting materials A and B are joined at their ends, forming a loop, and their junctions held at different temperatures, a current will flow through the loop. This is called a thermoelectric current. If this loop is broken as in Figure 2.3a, one can measure the potential difference ΔV_{AB} driving this current. We define the differential thermoelectric power S_{AB} as [34]

$$S_{AB} = \frac{dV_{AB}}{dT} \tag{2.4..1}$$

This differential thermoelectric power is the difference between the absolute thermoelectric power for each material, that is $S_{AB} = S_A - S_B$. The thermoelectric power is also known

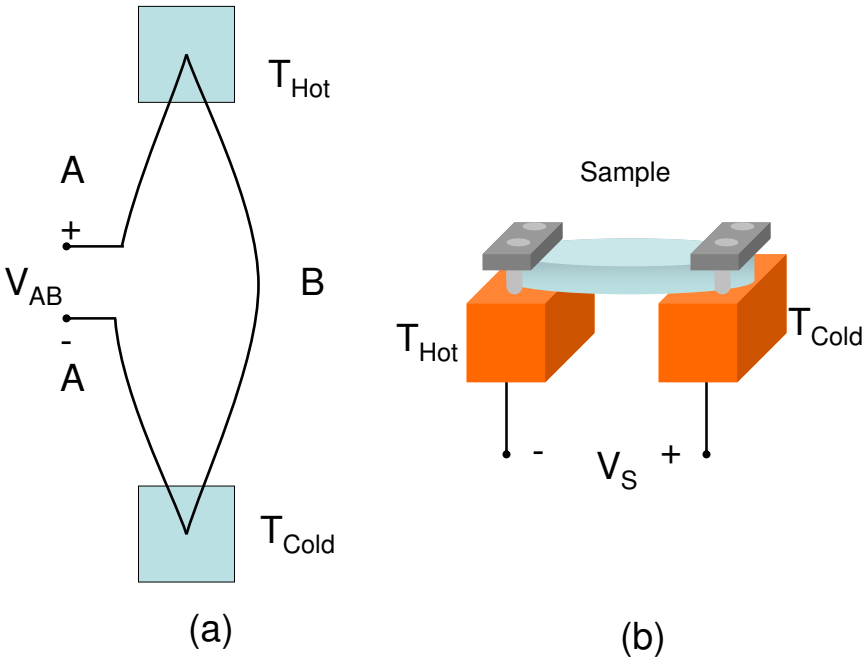

FIGURE 2.3: Seebeck voltage (a) and Seebeck measurement system. In (a), A and B are two different conducting materials. The voltage V_{AB} arises as a result of the temperature gradient. The voltage polarity in (b) has been flipped from (a) to follow the sign convention that n-type materials have a negative Seebeck coefficient.

as the Seebeck coefficient, and is a material property. The most common unit for the Seebeck coefficient is μV/K.

The Seebeck effect arises from a concentration gradient in the carrier concentration as a result of a temperature gradient. Suppose we have a piece of material which is in thermal equilibrium. Since the temperature is the same everywhere in the material, then the carrier concentration should also be the same. If we now heat one side of the material, there will be more thermally generated carriers on that side than the cold side, creating a carrier concentration gradient. Carriers will then diffuse from the high concentration area to the low concentration. This will cause an accumulation of charge at the cold end of the sample, creating an electric field which opposes the diffusion of more carriers from hot end to cold end.

We can determine the type of majority carrier in a material by measuring the sign of the voltage resulting from this electric field. If the material is n-type, then electrons will have diffused from the hot to the cold end. The resulting electric field will point from hot to cold to stop more electrons from diffusing, and thus $V_{Hot} - V_{Cold}$ will be positive. For holes, the electric field will have to point from cold to hot to oppose their diffusion, and $V_{Hot} - V_{Cold}$ will be negative. In this way a measurement of the voltage difference from hot to cold will tell you what the majority carrier type is.

We have defined the Seebeck coefficient to be $S = dV/dT$, which can be calculated from measurements as $\Delta V/\Delta T = (V_{Hot} - V_{Cold})/(T_{Hot} - T_{Cold})$ when the temperature difference is small compared to the temperature at either end. Since ΔT is always positive, the sign on S is determined by ΔV. This would give a negative Seebeck coefficient for holes and a positive coefficient for electrons. However, by convention we wish those signs to be opposite, so when measuring the Seebeck voltage we take ΔV to be $(V_{Cold} - V_{Hot})$. This gives n-type materials negative Seebeck coefficients and p-type materials positive coefficients.

It is interesting to note that highly resistive materials will generally give a negative Seebeck coefficient, even if they are weakly p-type [35]. In these materials the electron and hole concentration will be approximately equal. Electrons generally have a higher mobility than holes and will diffuse more easily, giving a negative Seebeck coefficient.

Now, measuring the Seebeck voltage will tell you the difference in Seebeck coefficients between the two materials involved, not the absolute coefficient for your sample. One possible solution to this problem is to use a superconductor as your second material. Superconductors do not display thermoelectric effects, thus $S_{Superconductor} = 0$, and you measure only the coefficient for your sample. The downside is this greatly limits the temperatures at which you can do your measurement. In our case, we will generally be measuring semiconductors, which tend to have high Seebeck coefficients ($> 100\mu V/\mathrm{K}$). These samples are placed on copper blocks, which have $S_{Cu} < 2\mu V/\mathrm{K}$ [36]. Since $S_{Sample} >> S_{Cu}$, we ignore the contribution to the coefficient from the copper blocks.

2.4.2 Experimental

Our Seebeck system is of in-house design, shown in Figure 2.3b. The sample pellet is placed across two copper blocks, one of which has a resistor in it for heating to provide the temperature gradient. The current to heat the resistor is supplied by a Keithley 2400 Digital SourceMeter. The induced voltage between the two blocks is measured by a Tektronix DM 5120 Digital Multimeter. The temperature difference between the copper blocks is found by measuring the voltage on a differential thermocouple between the two blocks. This voltage is measured by a Keithley 195A Multimeter. All of the multimeters and sources are controlled by a LabView program.

Before the sample is placed on the copper blocks, the blocks are cleaned with sandpaper, and then cleaned with methanol. Indium foil is then placed on the blocks to help make better contact between the blocks and the sample. The sample is also sanded down

to expose a new surface before measurements. After the blocks and sample have been cleaned and In contacts have been laid, the sample is placed on the contacts and then fastened in place with plastic strips which are attached to each block by screws. It is important to make sure the sample is fastened tightly to ensure good thermal and electrical contact, but be aware that the sample will break if it has been screwed down too tightly. The block cleaning procedure should be repeated between every measurement.

Before any samples are measured, a chromel wire is measured which has a known Seebeck coefficient of +20 μV/K. This is done to ensure that the polarity of the voltage measurements is correct, so that positive coefficients do in fact correspond to hole majority carriers, and also to make sure that the values measured are reasonable.

In a measurement, the block is heated to achieve a 5 Kelvin temperature difference, and then the heating current is turned off. Measurements are then recorded every few seconds until a temperature difference of approximately 1 Kelvin is reached, after which the measurements are not reliable. The Seebeck voltage is then plotted against the temperature difference, and a line is fitted to the data. The slope of this line gives the Seebeck coefficient.

2.5. Resistivity

2.5.1 Theory

Electrical resistivity ρ is an important material parameter to measure, as it will dictate the kinds of applications the material can be used for. The electrical conductivity σ of a material is the inverse of its resistivity, $\sigma = 1/\rho$. In a semiconductor, the resistivity can be controlled by adding dopants, and so resistivity measurements at different doping levels can be used to help verify whether a particular dopant species is producing the desired effects. In general, resistivity and conductivity are tensor quantities which depend

on the direction in which the current is applied. In a pressed powder sample, one expects the sample grains to be randomly oriented, and so we are effectively measuring an average over all the tensor components of the resistivity.

The resistivity of a sample could be measured by either a two-point or a four-point probe. In a two-point probe measurement, each probe acts as both a current and a voltage probe [35]. That is, the voltage drop across the sample is measured between the probes that are sourcing the current. In general the two-point probe is easier to implement, but will include contact and probe resistances in addition to the sample resistance. In a four-point probe measurement, two probes are used to source the current and another two probes are used to measure the voltage drop across the sample. Since the voltmeter will have a high input impedance ($\geq 10^{12}\Omega$), the current flowing through the voltmeter will be very small, causing the voltage dropped across the probe/contact resistances to be negligible. The only significant voltage drop measured will be that dropped across the sample. For this reason, four-point probe measurements are used to determine sample resistivity.

Resistivity is related to the resistance R of a sample by

$$\rho = R\frac{A}{l}, \tag{2.5..1}$$

where A is the cross sectional area of the sample and l is the length through which the current flows. This formulation is useful in when there is a uniform current flowing through a well defined A and l. The two contact geometries we use to measure resistivities are the collinear and Van der Pauw geometries; resistances are measured between nearest-neighbor contacts, and the current density is non-uniform.

The collinear contact arrangement is shown in Figure 2.4a. The current I flows between the outer two contacts (1 and 4), and the voltage drop V is measured between the inner two contacts (2 and 3). Contacts are placed as close to the middle of the sample

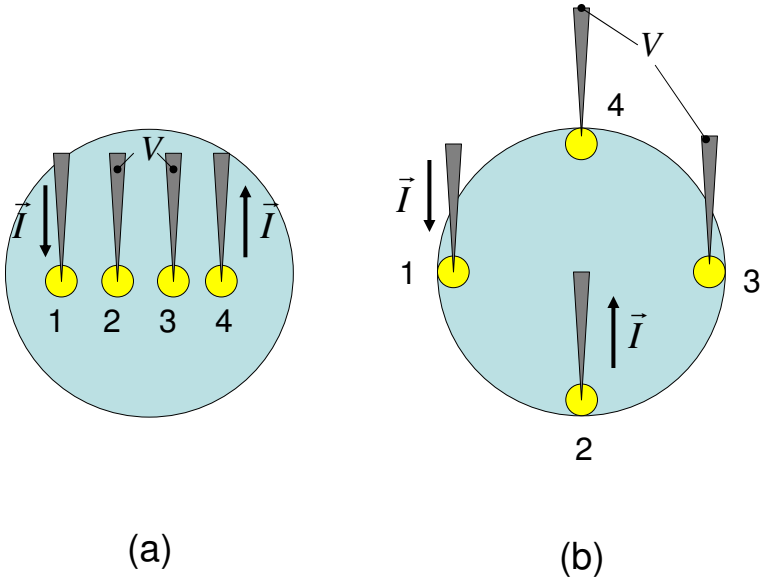

FIGURE 2.4: Collinear (a) and van der Pauw (b) contact arrangements. The contacts are typically 1 mm in diameter. In the collinear arrangement the contact spacing is 2 mm. In the van der Pauw arrangement the nearest neighbor contacts are 8 mm apart. With the current and voltage as shown in (b), the resistance $R_{12,34}$ can be determined.

as possible, and typical spacing between contacts ranges from 0.5 to 1.5 mm [35]. In general, the contacts will be equally spaced. For a sample which is infinitely wide and infinitely thick, the resistivity in the collinear geometry can be found by

$$\rho = 2\pi s \frac{V}{I}, \tag{2.5..2}$$

where s is the spacing between contacts [35].

Real samples will not have infinite dimensions, and so correction factors must be introduced. For collinear contacts, this is accomplished by multiplying Equation 2.5..2 by

the correction factor F.

$$\rho = 2\pi s F \frac{V}{I} \tag{2.5..3}$$

If sample thickness is on the order of the probe spacing, then F can be written as a product of three independent factors

$$F = F_1 F_2 F_3. \tag{2.5..4}$$

F_1 corrects for sample thickness, F_2 for lateral sample dimensions, and F_3 for placement of the probes relative to the sample edges.

In addition to depending on the sample thickness, the functional form of F_1 depends on whether the sample is measured on an insulating or conductive substrate. The substrates we use for measurement are insulating, and so F_1 can be found by

$$F_1 = \frac{t/s}{2\ln\left[\sinh\left(t/s\right)/\sinh\left(t/2s\right)\right]}, \tag{2.5..5}$$

where t is the sample thickness [35]. For conducting substrates, sinh is replaced with cosh. A plot of F_1 vs. t/s is shown in Figure 2.5. For our samples the thicknesses are between 1 and 2 mm, and the contact spacing is 2 mm, which gives $F_1 \sim 0.5$.

For a circular sample of diameter D, F_2 is given by

$$F_2 = \frac{\ln(2)}{\ln\left(2\right) + \ln\left[\frac{(D/s)^2+3}{(D/s)^2-3}\right]}. \tag{2.5..6}$$

For $D \geq 40s$, F_2 goes to 1. For our samples D is 12.7 mm and s is 2 mm, giving $F_2 \sim 0.8$. F_2 vs. D/s is shown in Figure 2.6.

F_3 corrects for edge effects, and is also dependent on whether the substrate is conducting or insulating. If the distance d from the edge of the sample to the contacts is $\geq 3s$, then F_3 is approximately 1. In our samples, this is true when measuring perpendicular

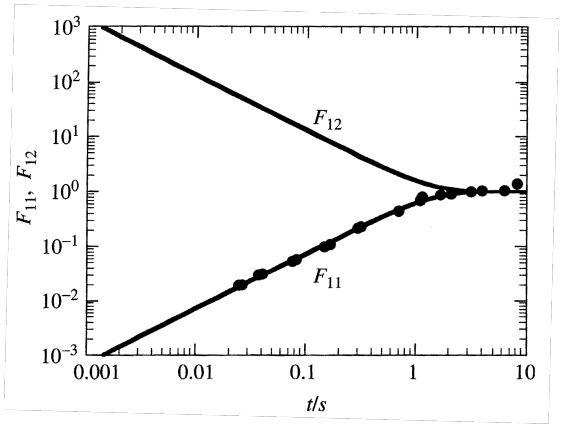

FIGURE 2.5: Correction factor F_1. F_{11} is used for insulating substrates, F_{12} for conductive substrates. Image taken from Schroder [35]

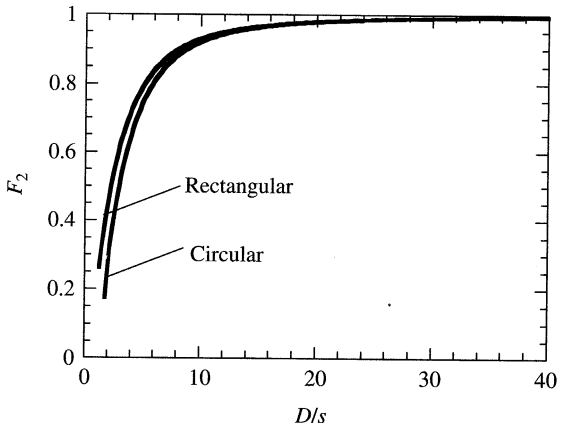

FIGURE 2.6: Correction factor F_2. Image taken from Schroder [35]

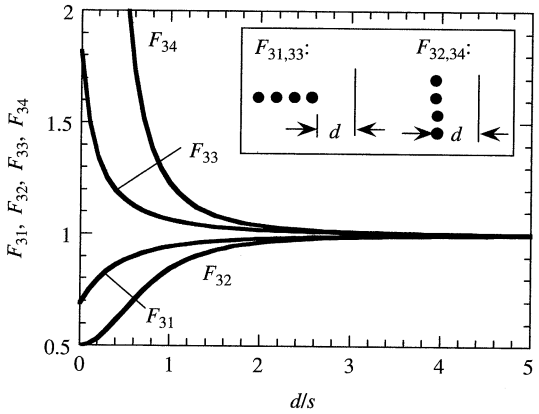

FIGURE 2.7: Correction factor F_3. F_{31} and F_{32} are for insulating substrates, F_{33} and F_{34} are for conductive substrates. Image taken from Schroder [35]

to the line of contacts. From the end contacts to the nearest edge is approximately $1.5s$, giving F_3 between 0.9 and 1. F_3 vs. d/s is shown in Figure 2.7. For our samples F_3 will be closer to 1 than to 0.9, and so we will assume it is 1 for simplicity.

Van der Pauw gave a method [37] for determining the resistivity of an arbitrarily shaped sample, given the following conditions: (a) the contacts are at the circumference of the sample, (b) the contacts are sufficiently small, (c) the sample has uniform thickness, and (d) the surface of the sample is singly connected, *i.e.*, the sample does not have isolated holes.

Figure 2.8 shows an arbitrarily shaped sample with four contacts. We will assume that it satisfies the four criteria above. Define the resistance $R_{ab,cd}$ as

$$R_{ab,cd} = \frac{V_{cd}}{I_{ab}}. \tag{2.5..7}$$

where the current I_{ab} flows from contact a to contact b, and the voltage V_{cd} is the voltage difference between contact c and contact d. The resistivity of the sample is given by [37]

$$\rho = \frac{\pi}{\ln(2)} t \frac{R_{12,34} + R_{23,41}}{2} f \tag{2.5..8}$$

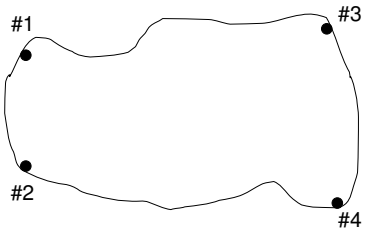

FIGURE 2.8: Arbitrary sample for four-point probe resistivity measurement. The resistance $R_{12,34}$ is defined to be V_{34}/I_{12}, where I_{12} is a current flowing between contacts #1 and #2, and V_{34} is the voltage difference between contacts #3 and #4.

where t is the thickness of the sample and f is a function of the ratio $R_{12,34}/R_{23,41}$ which satisfies the relation

$$\frac{R_{12,34} - R_{23,41}}{R_{12,34} + R_{23,41}} = \frac{f}{\ln(2)} \operatorname{arccosh}\left(\frac{\exp\left[\ln(2)/f\right]}{2}\right) \tag{2.5..9}$$

The dependence of f upon $R_{12,34}/R_{23,41}$ is given in Schroder Figure 1.9 [35].

When the contacts are placed symmetrically on the sample sample and $R_{12,34} = R_{23,41}$, then $f = 1$ and Equation 2.5..8 becomes

$$\rho = \frac{\pi}{\ln(2)} t R_{12,34} \equiv 4.532 t R_{12,34} \tag{2.5..10}$$

Figure 2.4b shows our van der Pauw contact arrangement. Even when the contacts are placed symmetrically on the sample, the various $R_{ab,cd}$ will generally not be equal due non-uniformities in the sample. It is useful to obtain an average resistivity by including the remaining two contact permutations and reversing the current for all measurements

[38]. The resistivity is then found by

$$\rho = \frac{\pi t}{8\ln(2)}(R_{21,34} - R_{12,34} + R_{32,41} - R_{23,41} + R_{43,12} - R_{34,12} + R_{14,23} - R_{41,23}) \quad (2.5..11)$$

The above equations are derived assuming that the contacts are of negligible size and located on the periphery of the sample. Van der Pauw gave a correction for contacts of finite size on a circular sample [37]. For each contact of finite size, the percent change in the resistivity $\Delta\rho/\rho$ is given by

$$\frac{\Delta\rho}{\rho} = -\frac{1}{16\ln 2}\frac{d^2}{D^2} \quad (2.5..12)$$

where d is the diameter of the contact and D the diameter of the sample. Since there will be four contacts, this percent change must be multiplied by 4. The overall correction factor for four contacts is then

$$1 - \frac{1}{4\ln 2}\frac{d^2}{D^2} \quad (2.5..13)$$

For a 1 mm contact on a 12.7 mm disk gives a correction of 0.998. Since this correction is so small for our samples, it will be ignored.

Cold-pressed pellets will generally not achieve 100% theoretical density, and will thus contain non-conducting pores. These pores will increase the measured resistivity of the sample, and must be corrected for. In this work we will use the minimum solid area model presented by Rice [39].

The minimum solid area model assumes that any flux through a material is limited by the smallest cross-sectional area through which it passes. It has been found [39] that for a volume fraction of pores $p <\sim 0.3$ the correction factor from this model has an exponential form:

$$\rho_{actual} = \mathrm{e}^{-bp}\rho_{measured} \quad (2.5..14)$$

where b is a parameter which depends on the nature of the pores. We will assume that we have spherical pores in our pellets, in which case $b = 3$. Our pellets are typically 80% dense, which gives a volume fraction of pores $p = 0.2$. The correction factor for this density is $e^{3*0.2} \approx 0.549$.

2.5.2 Experimental

Four-point probe resistivity measurements are taken on a Lakeshore Hall effect system. Both collinear and Van der Pauw contact geometries are used. Contacts are made of evaporated gold, deposited directly on freshly cleaned sample surfaces. Sample thicknesses are typically 1 to 2 mm. In both contact geometries, I-V curves are taken for each nearest neighbor contact pair to check that contacts are Ohmic.

In the collinear geometry, circular contacts 1 mm in diameter are placed 2 mm apart, measured from the center of the contacts. Current is sourced between probes #1 and #4, the voltage drop measured between probes #2 and #3, and the resistance is determined. The direction of the current is then reversed and the measurement repeated. The two resistances are then averaged. This resistance is used to calculate the resistivity from Equation 2.5..3, using appropriate correction factors.

In the Van der Pauw geometry, contacts are placed evenly around the edge of the sample. The distance to the nearest neighbor contact is 8 mm. Eight sets of measurements are done, to find the resistances $R_{12,34}$, $R_{23,41}$, $R_{34,12}$, and $R_{41,23}$ and then reversing the current for each measurement. An average resistivity is then found by Equation 2.5..10.

3. RESULTS AND DISCUSSION

3.1. Impurity phases

3.1.1 XRD and physical characteristics

The most common impurities found during $SnZrS_3$ synthesis are SnS and ZrS_2. The largest peaks of ZrS_2 and SnS_2 tend to be very close to each other, or are obscured by $SnZrS_3$ peaks, making XRD identification of which impurity phase is present difficult at times. We synthesized both materials to find distinguishing physical characteristics for visual identification. When $SnZrS_3$ is formed under very sulfur rich conditions, ZrS_3 will form. For Sn_2S_3 the only observed impurity phases have been SnS and SnS_2.

ZrS_2 forms a dark red powder. When found in $SnZrS_3$, the ZrS_2 powder is interspersed with the $SnZrS_3$ powder, which is dark grey. When interspersed like this, the ZrS_2 takes on more of a purple hue. Because the two powders are mixed, it is very difficult to separate them. The XRD pattern for ZrS_2 is shown in Figure 3.1. This sample was sintered at 800 °C for 12 hours, which are the same oven conditions we make $SnZrS_3$ in. This yielded a quite pure powder.

SnS_2 forms a bright orange plate-like structure, which leads to easy visual identification between ZrS_2 and SnS_2. SnS_2 tends to accumulate on tube walls during synthesis, allowing some mechanical separation. However, in Sn_2S_3 synthesis, some SnS_2 will be interspersed among the Sn_2S_3 powder, preventing complete separation. When made at 800 °C for 12 hours, the result was primarily SnS_2 with a small amount of Sn_2S_3. The XRD pattern is shown in Figure 3.2.

The measured peak intensities very poorly fit the peak intensities indicated by the PDF from [14]. However, there seems to be some regularity to the mismatch. The (0 0 X) peaks tend to be at a much higher intensity than would be expected, and the (1 0

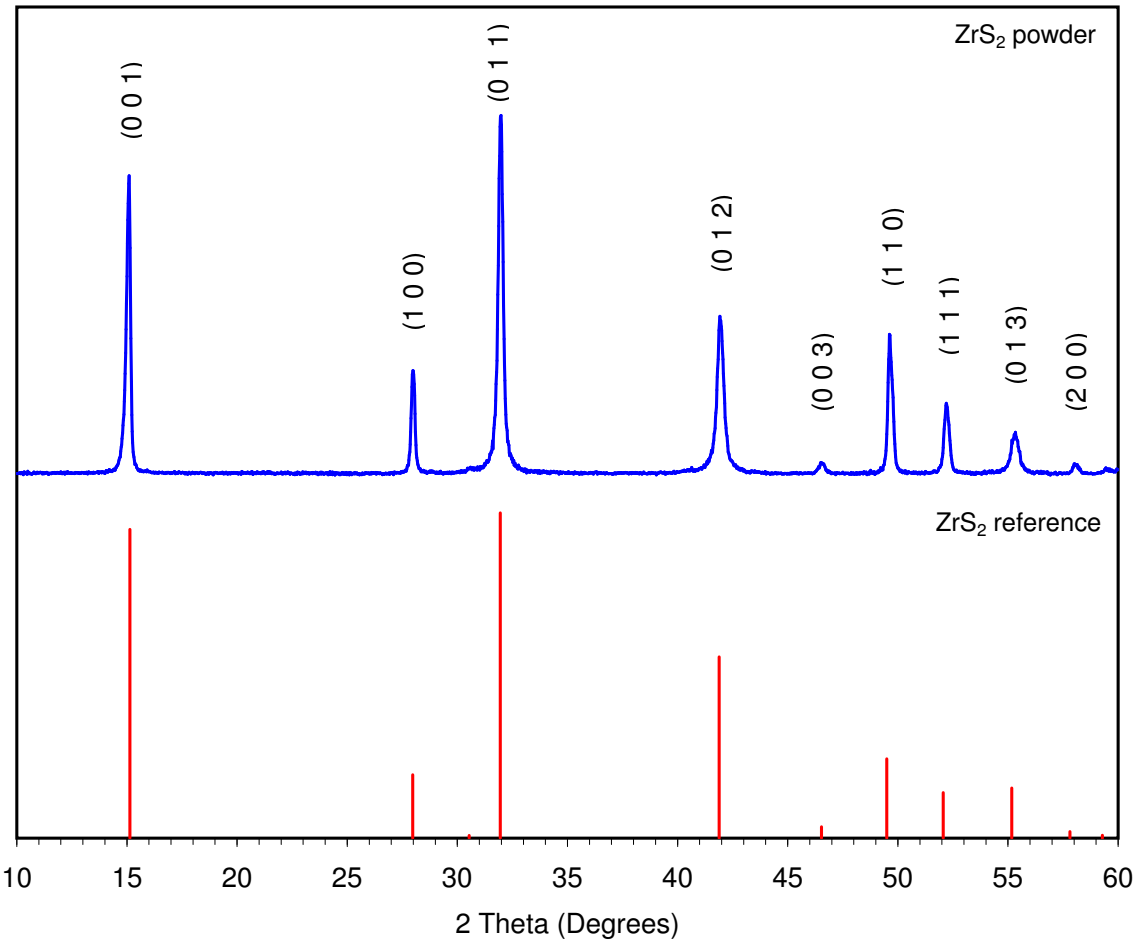

FIGURE 3.1: ZrS_2 XRD pattern. The reference pattern is from [40]

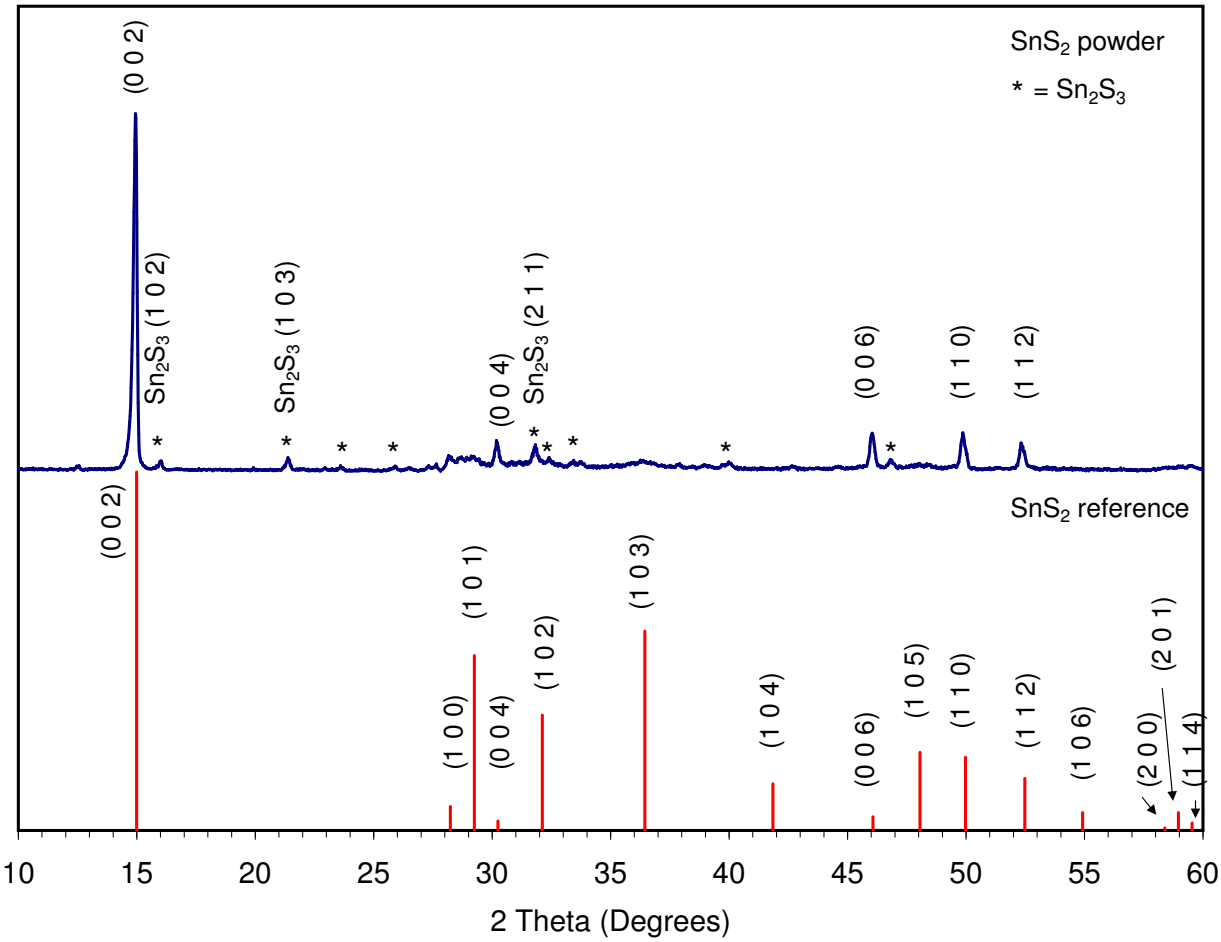

FIGURE 3.2: SnS_2 XRD pattern. The reference pattern is from [14]

X) peaks are at a much lower intensity, becoming entirely suppressed at large 2θ. This likely means that the powder is not randomly oriented, instead it seems that there is a preferential orientation along the (0 0 X) direction. This may be due to SnS_2's layered structure.

SnS has a metallic appearance. It will tend to accumulate on tube walls during synthesis of $SnZrS_3$ and Sn_2S_3, making mechanical separation of the bulk of the impurity phase possible. The XRD pattern for SnS synthesized at 800 °C for 12 hours is shown in Figure 3.3. This sample had a small Sn_2S_3 impurity phase which was mostly removed

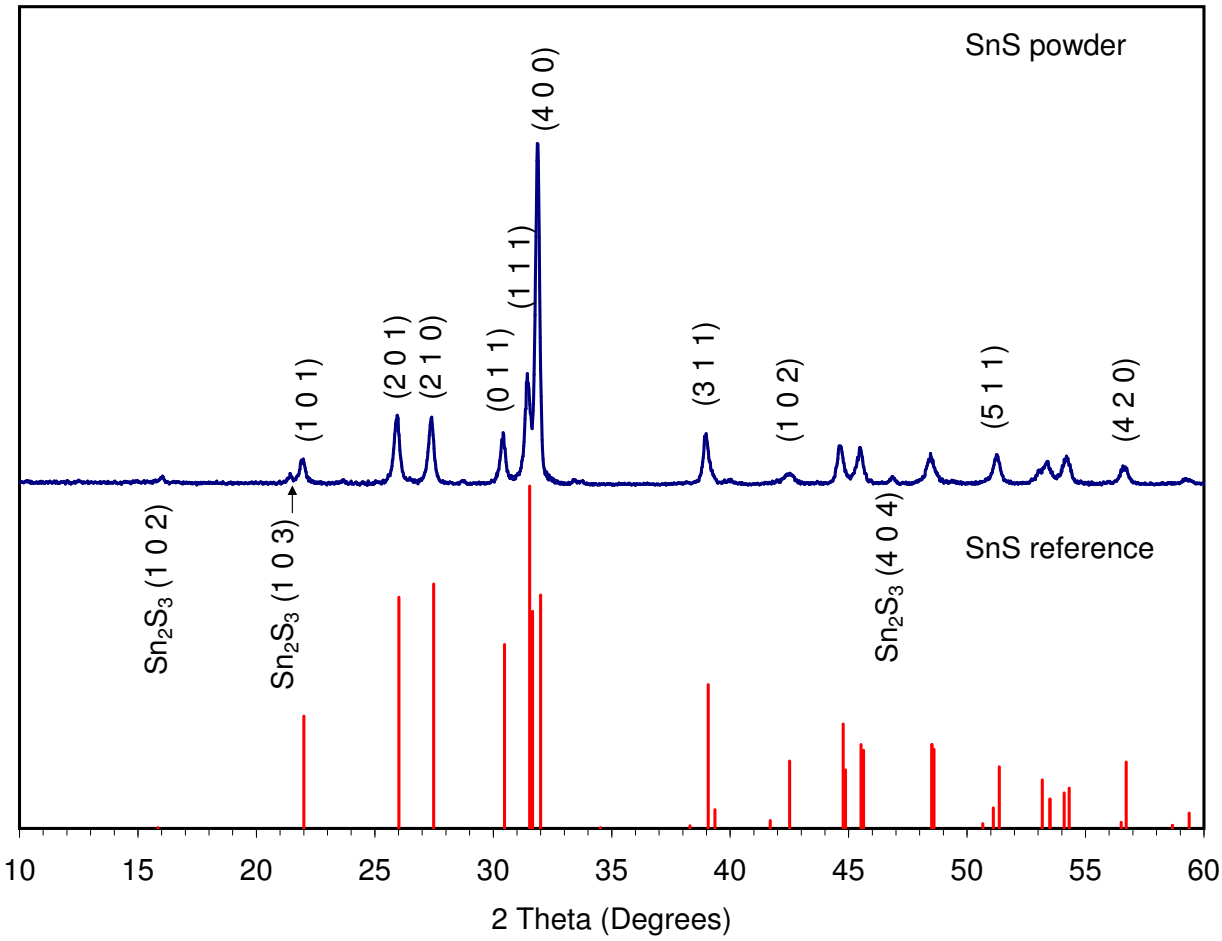

FIGURE 3.3: SnS XRD pattern. The reference pattern is from [7]

before XRD analysis.

ZrS_3 forms a red, very low density material which is almost sponge-like in texture. The elemental powders for most materials in this work will occupy perhaps a tenth of the silica tube prior to sintering. After sintering they will tend to occupy 10-20% of the tube. For ZrS_3, if the elemental powders occupied 10% of the tube, the resulting ZrS_3 will occupy nearly 50% of the tube space. When grinding in a mortar and pestle, the powder will tend to clump together. When appearing as an impurity phase in $SnZrS_3$, ZrS_3 is bright red and is interspersed with the $SnZrS_3$ powder. ZrS_3 tends to be somewhat more

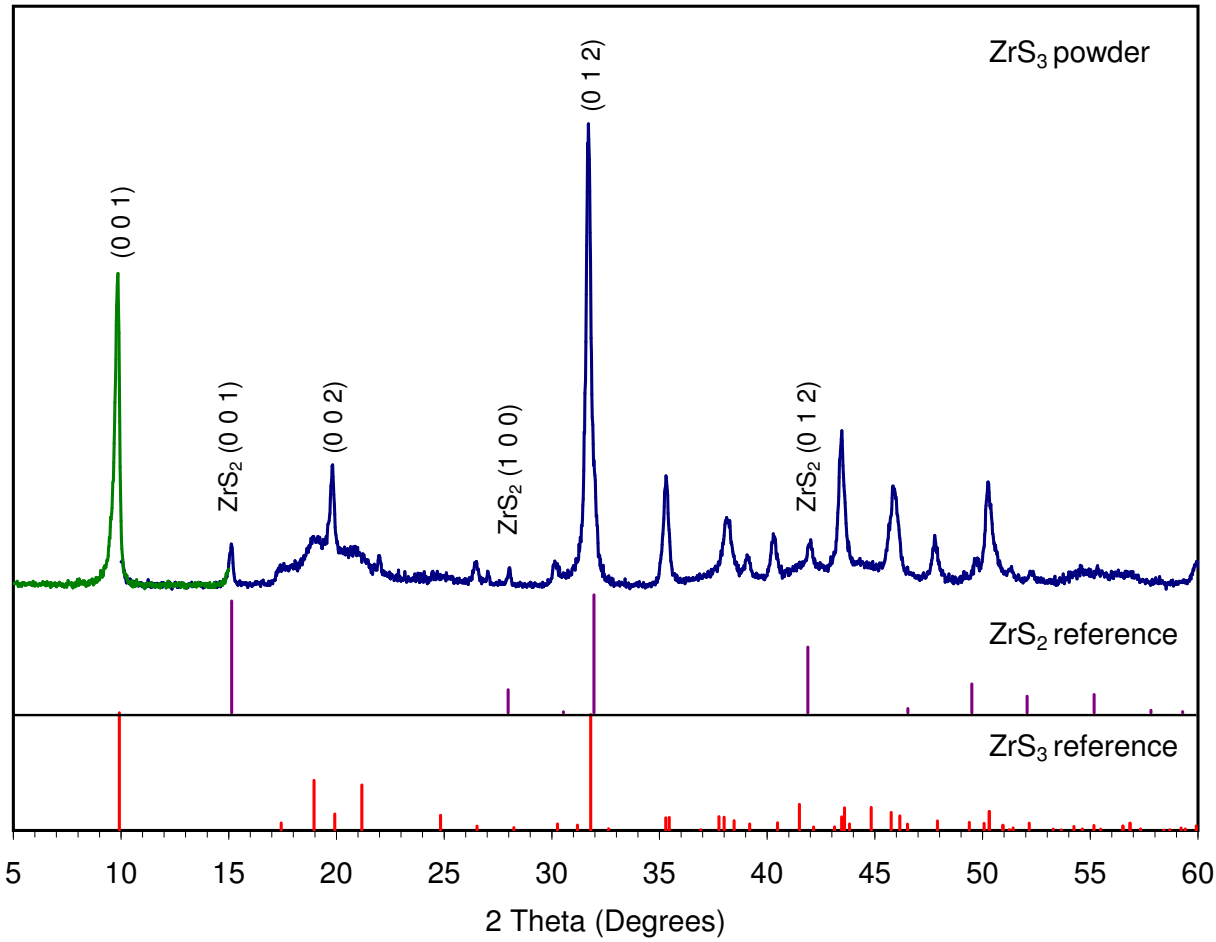

FIGURE 3.4: ZrS_3 XRD pattern. The green data is from a measurement from 5-15° 2θ. The blue data is from a measurement over 10-60° 2θ. The reference pattern for ZrS_3 is from [23]. The reference pattern for ZrS_2 is from [40]

segregated within the $SnZrS_3$ powder than is ZrS_2, and is a much brighter red compared to the purple hue that ZrS_2 has in $SnZrS_3$.

Figure 3.4 shows the XRD pattern for ZrS_3 grown at 900 °C. This pattern was made in two separate runs, as it was not initially realized the largest ZrS_3 peak is just below the normal 10° starting angle. There is a ZrS_2 impurity phase present in this sample. There are also low, broad humps through some sections of the pattern, which are possibly indicative of an amorphous phase.

3.1.2 Optical and Transport properties

Reported bandgaps for ZrS_2 and SnS_2 are around 1.7 eV and above [16, 18]. Bandgaps for $SnZrS_3$ and Sn_2S_3 appeared to be around 1.3 eV or lower, which means that near the absorption edges for these materials, ZrS_2 and SnS_2 are transparent. As a result, these impurities will not affect optical measurements to determine the bandgaps of $SnZrS_3$ and Sn_2S_3. As such, we did not make optical measurements for the disulfides. Reported bandgaps for SnS vary from 0.9 up to 1.7 eV, which covers the range in which we expect to find the bandgaps for $SnZrS_3$ and Sn_2S_3. We took diffuse reflectance measurements on SnS to get a better idea of what bandgap we expect to see in our SnS impurity phases.

Figure 3.5 shows the reflectivity and K/S data for SnS. There is a slight discontinuity between the NIR data set and the UV-Vis data set. This was also seen in a Sn_2S_3 sample measured immediately after the SnS sample. Data from other Sn_2S_3 samples shows that the NIR data is more consistent than the UV-Vis data, and so we take our bandgaps for SnS from the NIR data. The bandgap as found by the method described by Fochs [28] from the reflectivity data is 1.11 eV. Figure 3.6 shows the $((K/S)E)^2$ and $((K/S)E)^{1/2}$ versus energy plots. LCAO calculations have shown SnS to be an indirect semiconductor [12], so the $((K/S)E)^{1/2}$ plot is used to find bandgap values. The bandgap found from this plot was 1.10 eV. This value agrees with the reported range of 0.9-1.1 eV for indirect gaps for SnS [8].

Seebeck measurements indicate ZrS_2 has n-type conductivity and SnS has p-type conductivity, with Seebeck coefficients of -600 μV/K and +520 μV/K respectively. These results both agree with majority carrier types found in literature. SnS_2 was measured to have p-type conductivity as well, which does not agree with most literature. The measured Seebeck coefficient for SnS_2 was in the range of 1600-1700 μV/K. Our SnS_2 samples were not phase pure, which could explain the lack of agreement. The large magnitude of the Seebeck coefficient indicates that the SnS_2 sample was highly resistive.

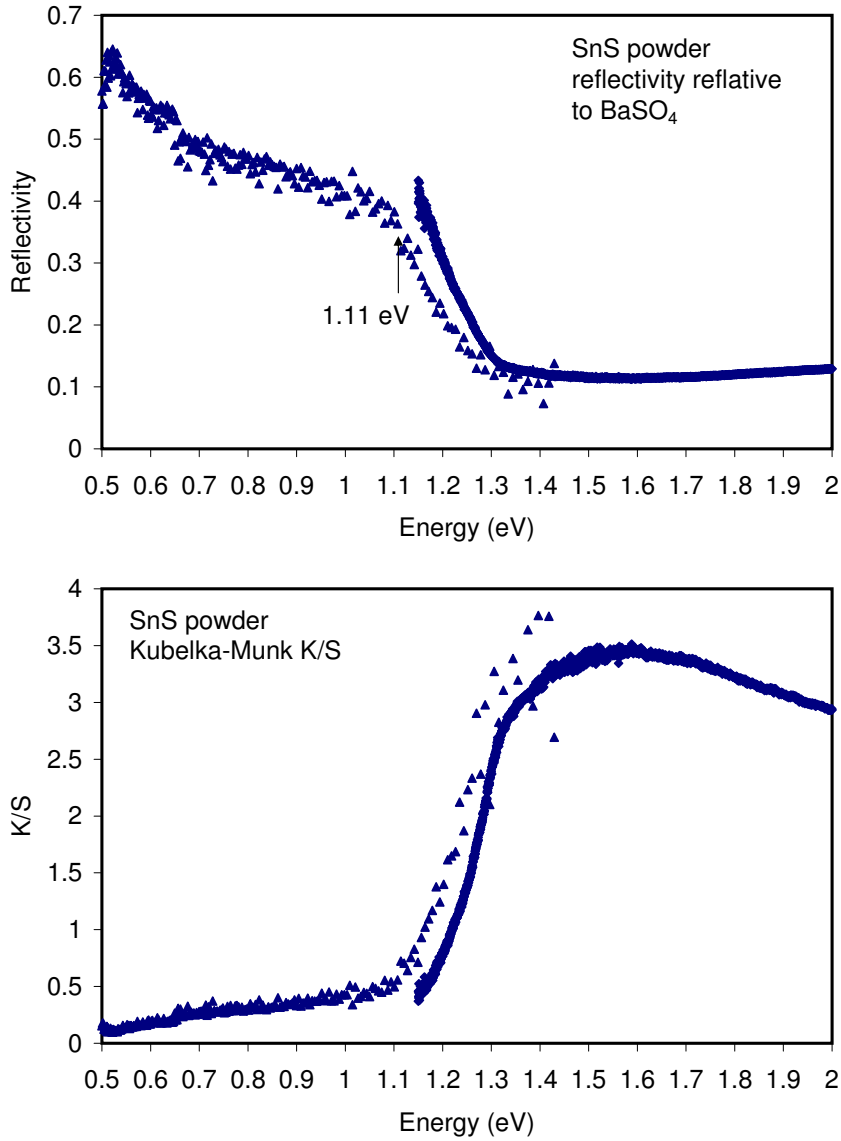

FIGURE 3.5: SnS diffuse reflectivity (top) and K/S (bottom) plots. Bandgaps as found via [28] are indicated in the reflectivity plot. The triangular data points are from the NIR measurement, and the diamond data points are from the UV-Vis measurement.

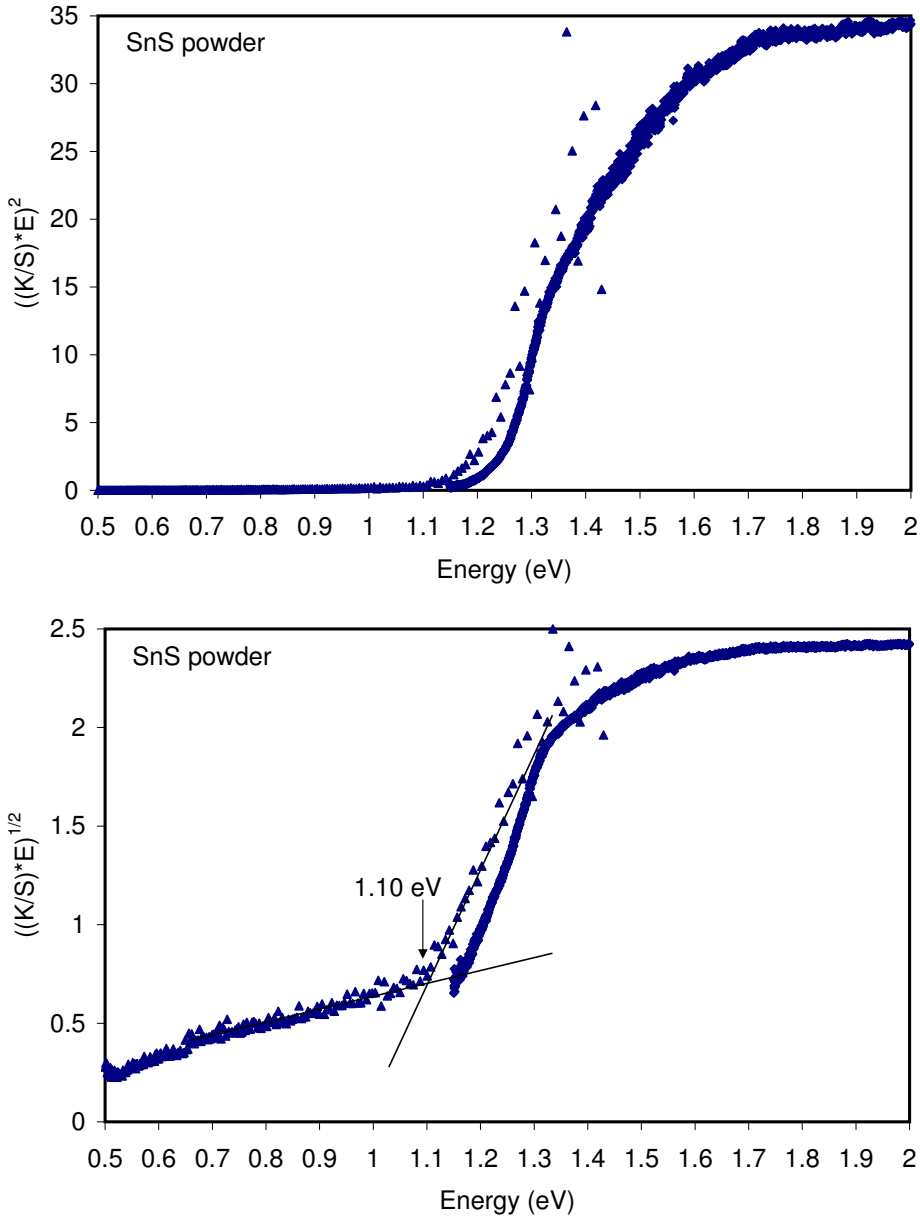

FIGURE 3.6: SnS $((K/S)E)^2$ (top) and $((K/S)E)^{1/2}$ (bottom) vs. energy plots. The bandgap found in the $((K/S)E)^{1/2}$ plot is indicated. The triangular data points are from the NIR measurement, and the diamond data points are from the UV-Vis measurement.

3.2. $SnZrS_3$ and Sn_2S_3

3.2.1 Synthesis and Structure

It was found that at all synthesis temperatures up to 1000 °C, a stoichiometric mix of tin, zirconium, and sulfur will result in a combination of $SnZrS_3$, ZrS_2, and SnS. The amount of $SnZrS_3$ present is maximized at 900 °C, but the two impurity phases are still present. As the synthesis temperature is lowered, the impurity levels increase. At a temperature of 500 °C the reaction products are predominantly ZrS_2 and SnS, and there is very little $SnZrS_3$ present. Above 900 °C there is a rise in impurity levels. Figure 3.7 shows XRD patterns for growths between 825 °C and 1000 °C.

The largest SnS XRD peak is obscured by peaks already present in the $SnZrS_3$ pattern, and so in small quantities it is sometimes difficult to detect in XRD patterns. As a result, in analyzing our XRD patterns for our early synthesis attempts, we thought there was only a ZrS_2 impurity phase. It was hypothesized that the ZrS_2 impurity was a result of the preferential loss of Sn, either through the Sn powder being lost in the mixing process before being sealed in the synthesis tube, or from deposition of Sn on the tube walls during sintering. The Sn powder that we used had a tendency to stick to the weighing paper and to get blown off into the air from the weighing paper while transporting it to the mortar for mixing. To minimize the effects from this we switched to a coarser Sn powder. There was less Sn that stuck to the weigh paper, and there wasn't a visually noticeable loss of Sn during transportation, but no noticeable change in the XRD patterns was effected. To try to reduce the effects of Sn deposition on the tube walls, we tried adding excess Sn to tube. At 15% excess Sn we no longer had a ZrS_2 impurity, but we did have Sn metal peaks in the XRD pattern. It was assumed that we would then be able to reduce the Sn excess to remove the Sn impurity, leaving just $SnZrS_3$. However, as the Sn excess was reduced we again had ZrS_2 being produced.

After making the known impurity phases by themselves to attempt visual identifica-

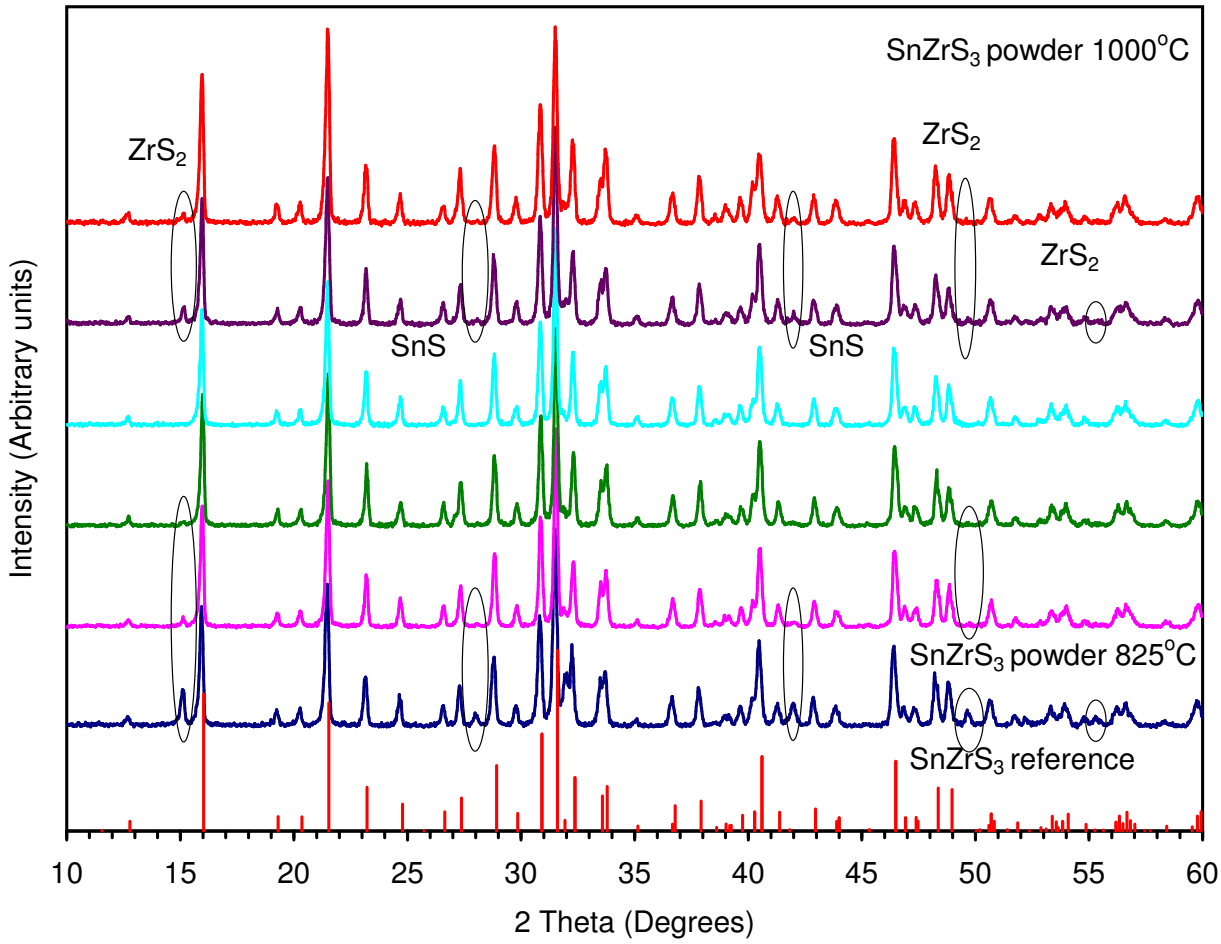

FIGURE 3.7: $SnZrS_3$ XRD patterns for different sinter temperatures. The top pattern is from a 1000 °C synthesis. Each lower pattern reduces the temperature by 25 °C, until the bottom pattern is from an 825 °C synthesis. The reference pattern is from [1].

tion of impurities, it was realized that there was in fact a SnS impurity in addition to the ZrS_2 in the stoichiometric syntheses of $SnZrS_3$. While the SnS is hard to identify in small quantities in the XRD pattern, it is very easy to indentify visually in the synthesis tube as a metallic deposit on the tube wall. It is hypothesized that these impurities arise together because of local deficiencies in the sulfur content during synthesis. Sulfur becomes a gas at approximately 445 °C, which is well under all of our synthesis temperatures. Both Sn and Zr have boiling points of over 2000 °C, and so are not gaseous during synthesis. When sulfur becomes a gas during the synthesis, it will spread itself around the volume of the tube. Since the Zr and Sn are localized to a small extent of the tube, if a stoichiometric mix of Sn, Zr, and S are put in, then the Sn and Zr will locally experience a S concentration far below that of stoichiometric $SnZrS_3$. If this is true, then increasing the sulfur content should increase the yield of $SnZrS_3$.

A sulfur excess of 8% was first tried (for a stoichiometry of $SnZrS_{3.25}$), at a synthesis temperature of 900 °C. This entirely eliminated the ZrS_2 and SnS impurities, but produced ZrS_3 in addition to the desired $SnZrS_3$. At both 3% and 2% excess sulfur, pure $SnZrS_3$ was sometimes obtainable, but sometimes the synthesis will result in a mix of $SnZrS_3$ and ZrS_3. The result appears to depend very much on the conditions in the oven, which were not stable in the oven being used at the time. After changing ovens, it was found that $SnZrS_3$ can be made phase pure at 800 °C with a sulfur excess of 1.67% ($SnZrS_{3.05}$). Figure 3.8 shows the XRD pattern obtained for $SnZrS_3$ made with 1.67% excess S at 800 °C compared with the powder diffraction file (PDF) pattern, from [1].

Since Sn_2S_3 has a melting point of 760 °C [5] and we wish to sinter the material below its melting temperature, we first tried a sinter temperature of 750 °C for 12 hours, with a stoichiometric mixture of the elements. At this temperature, a mixture of Sn_2S_3 and SnS_2 was formed. At 725 °C a mixture of Sn_2S_3 and SnS was obtained. At 650 °C there was again a mixture of Sn_2S_3 and SnS, in about the same proportions as at

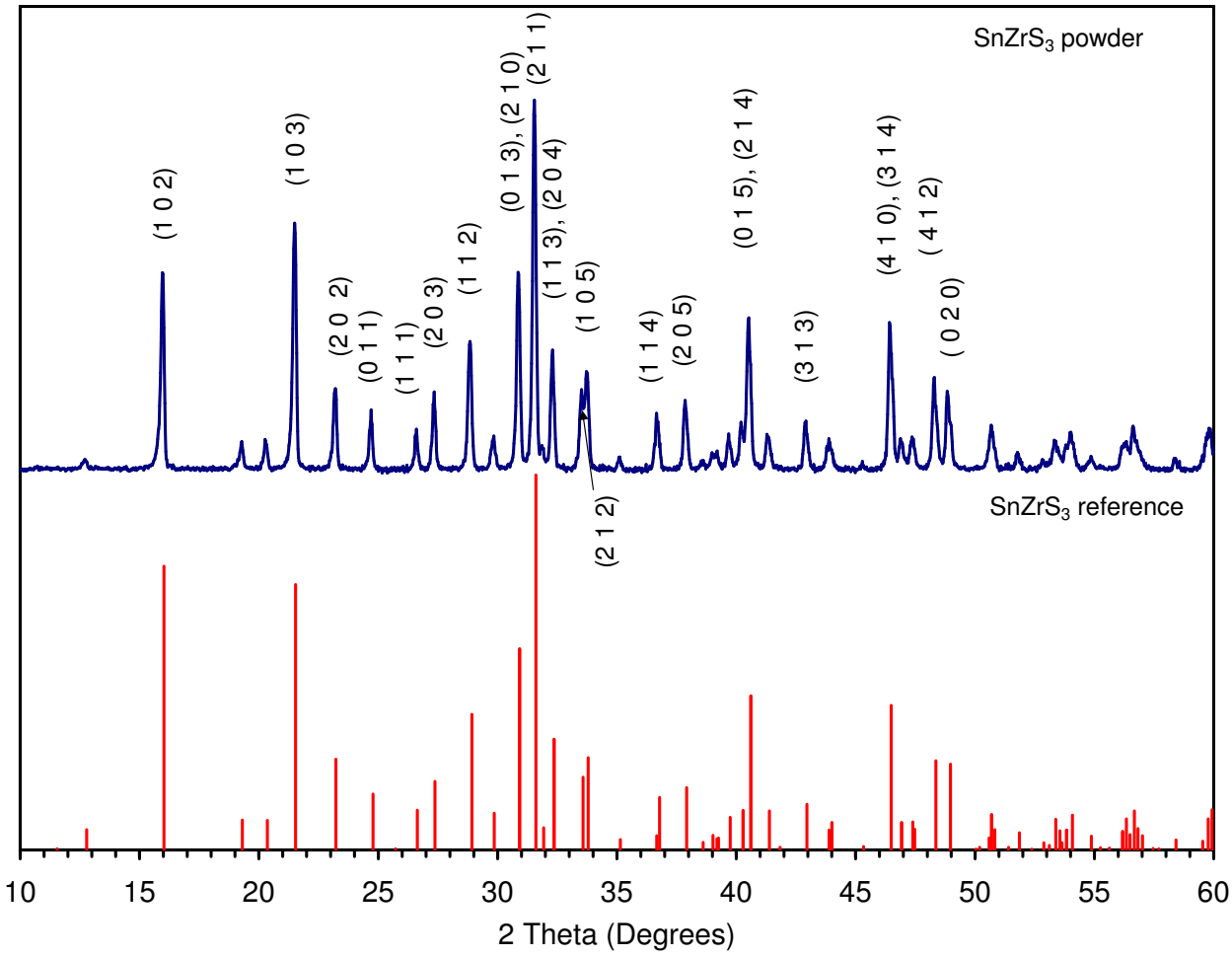

FIGURE 3.8: $SnZrS_3$ XRD pattern. The top pattern is measured, the bottom pattern is from [1].

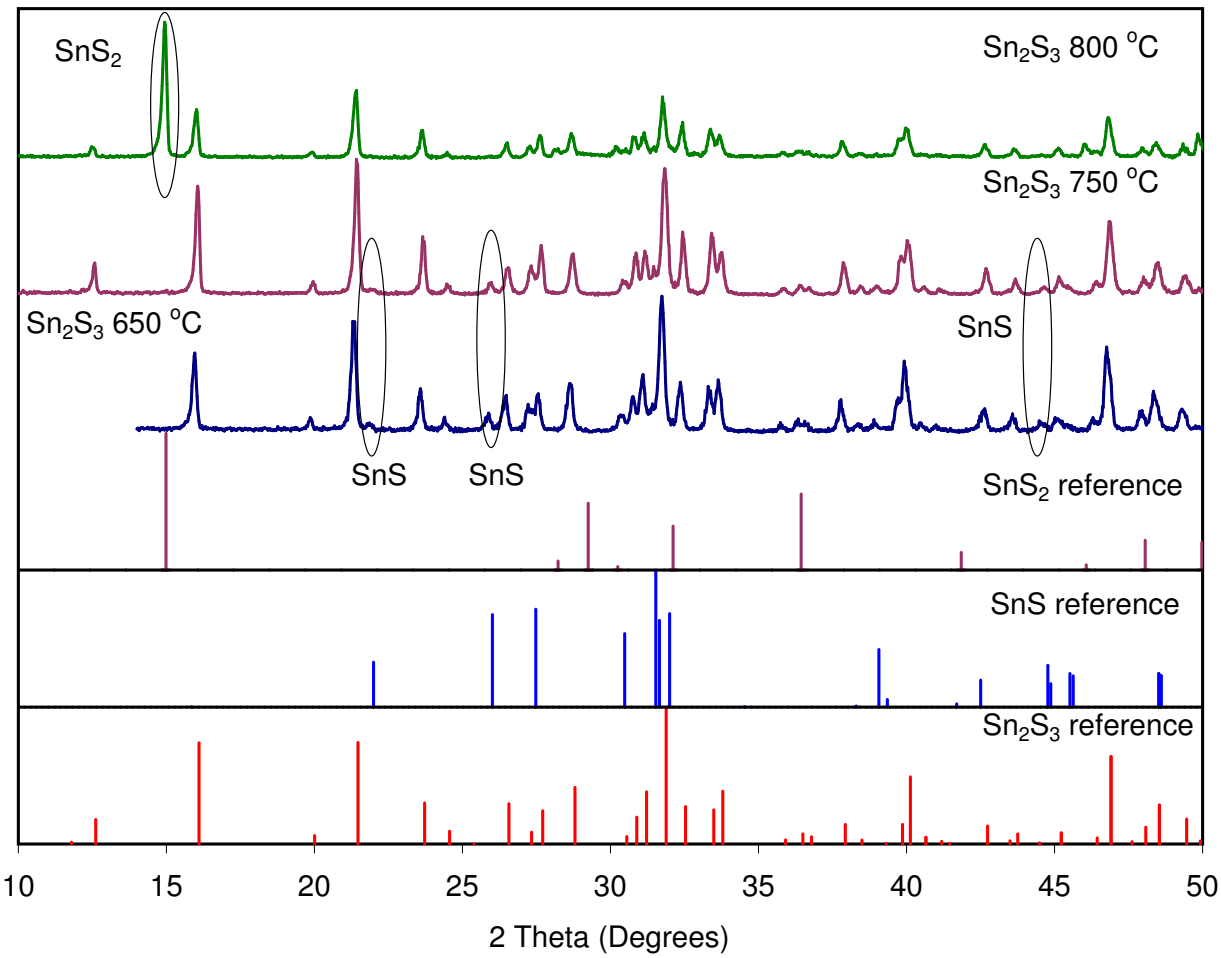

FIGURE 3.9: Sn_2S_3 XRD patterns for different sinter temperatures. The top (green)measured pattern was sintered at 750 °C, the middle (purple) pattern is at 725 °C, and the bottom (blue) pattern is at 650 °C. The reference patterns from top to bottom are SnS_2 [14], SnS [7], and Sn_2S_3 [41].

725 °C. These results are consistent with those of Moh [5], who found that from 650-750 °C mixtures of elemental Sn and S produced Sn_2S_3 and that from 750-850 °C the same mixtures produced Sn_2S_3 and SnS_2. Figure 3.9 shows the XRD patterns for Sn_2S_3 synthesized at 650 °C, 725 °C, and 750 °C. Since there was not any appreciable gain in sintering at 725 °C over sintering at 650 °C, we chose to continue our syntheses at the lower temperature.

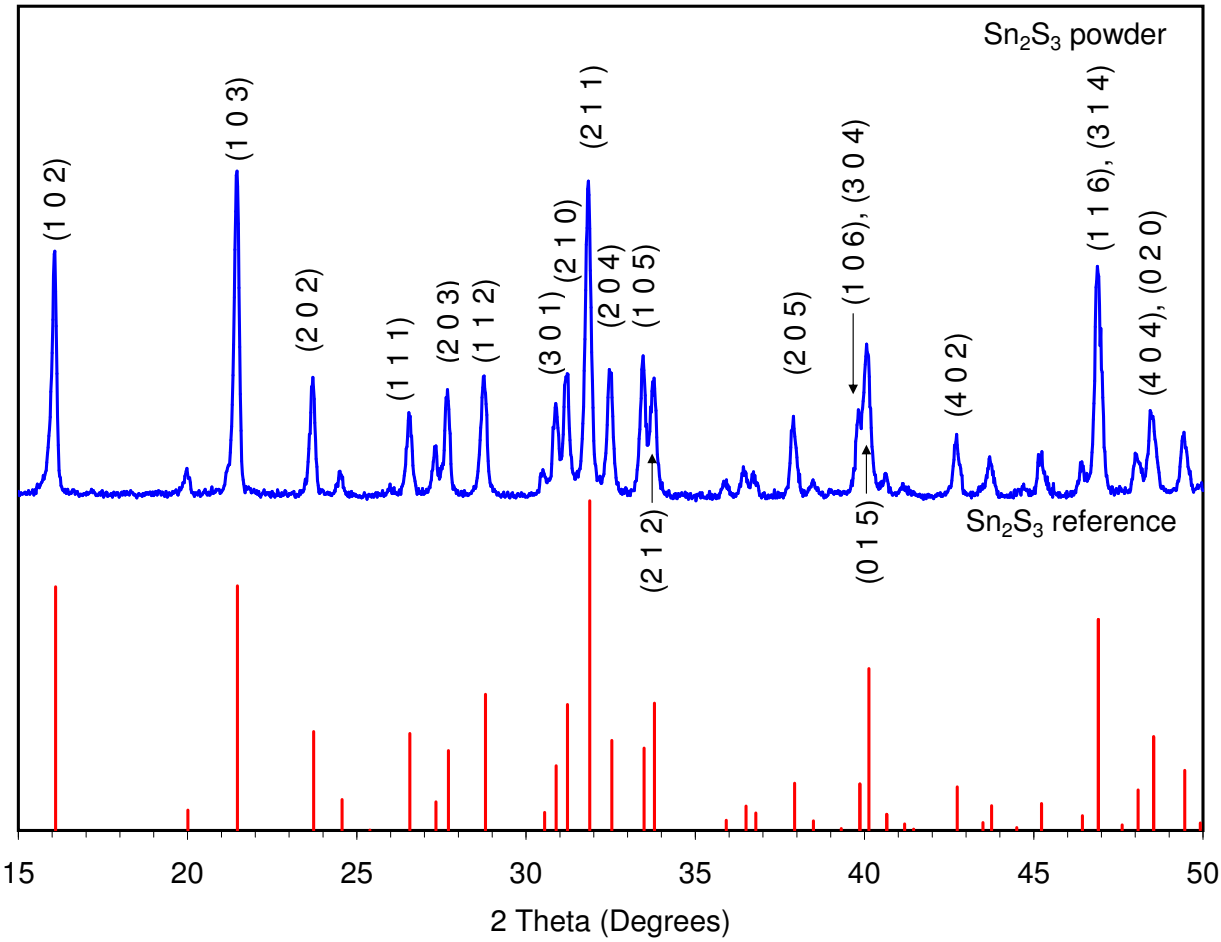

FIGURE 3.10: Sn_2S_3 XRD pattern. Synthesis at 650 °C for 12 hours, with 1.66% excess S. The reference patternis from [41].

For synthesis conditions which produce a mixture of SnS and Sn_2S_3, we would like to be able to simply add more S to cause the SnS to convert to Sn_2S_3. An excess of 1.67% S ($Sn_2S_{3.05}$) was tried at a sinter temperature of 650 °C for 12 hours. This resulted in a phase pure powder. The XRD pattern for this sample is shown in Figure 3.10. However, efforts to replicate this success under ostensibly the same conditions have failed. When excess S has been added to subsequent samples, an SnS_2 impurity phase is formed. When excess S is not added, SnS is present in the samples, and at times both SnS and SnS_2.

We believe that the reason for our lack of phase purity in the Sn_2S_3 system is the duration of our sinters. We sinter our samples typically for 12 hours. The sinter times reported by Moh [5] were at least 100 hours, and frequently much more than that. It is possible that the reactions to form SnS and SnS_2 happen relatively quickly, whereas the reaction to form Sn_2S_3 happens quite slowly.

The vacuum achieved seemed to have a significant effect on the phase purity for both $SnZrS_3$ and Sn_2S_3. When the Varian TMP was not available and we were only able to pump down to 10^{-3} Torr, I was unable to create phase pure materials. The higher vacuum of the TMP (10^{-6} Torr) greatly improved the purity of the samples.

3.2.2 Transport Properties

When made phase pure, the Seebeck coefficient for $SnZrS_3$ ranges from 600 to 700 μV/K, indicating that it is natively p-type. Early results had given a negative Seebeck coefficient, but in every sample of $SnZrS_3$ that we have measured a negative Seebeck coefficient there has been a ZrS_2 impurity phase. ZrS_2 is known to be n-type [18], and so could cause the $SnZrS_3$ sample to have a negative Seebeck coefficient.

Sn_2S_3 also appears to have a positive Seebeck coefficient, indicating p-type conductivity. The measured samples did contain SnS impurities, which may alter the Seebeck coefficient. The coefficient was measured to be +1000 μV/K. We would expect to see a Seebeck coefficient smaller in magnitude than that of $SnZrS_3$ due to the smaller resistivity for Sn_2S_3. It is possibly that non-stoichiometries in the measured sample caused the electrical properties to be altered.

The lowest measured electrical resistivity for $SnZrS_3$ has been 13 MΩcm. A resistivity of 216 kΩcm has been measured for Sn_2S_3 with evaporated gold contacts in a collinear arrangement. Single crystal resistivities of Sn_2S_3 have been reported to be 33 kΩcm [3], which is significantly lower than the bulk powder measurement.

3.2.3 Optical Properties

The diffuse reflectance spectra for several $SnZrS_3$ samples are shown in Figure 3.11. Bandgaps as found by the method described by Fochs [28] are indicated on this plot, which range from 1.16 eV to 1.21 eV. The K/S spectra as found through Equation 2.3..5 are also shown in Figure 3.11. Figure 3.12 shows the $((K/S)E)^2$ and $((K/S)E)^{1/2}$ versus energy plots for these spectra. Since $SnZrS_3$ has been calculated to be an indirect bandgap material, we use the $((K/S)E)^{1/2}$ to determine the bandgap. The bandgaps obtained from this plot range from 1.16 eV to 1.19 eV, which agrees with the values obtained from the reflectivity data.

Reflectivity and K/S spectra for Sn_2S_3 are shown in Figure 3.13. Bandgaps found from the reflectivity data range from 1.14 eV to 1.15 eV. Figure 3.14 shows the $((K/S)E)^2$ and $((K/S)E)^{1/2}$ versus energy plots for Sn_2S_3. Sn_2S_3 is calculated to have an indirect bandgap, and so we use the $((K/S)E)^{1/2}$ to extract bandgap values. The bandgaps found from this plot range from 1.15 eV to 1.16 eV. These values agree well with the bandgaps found from the reflectivity. In one of the spectra from the fiber optic system the reflectivities from the NIR lamp and the UV-Vis lamp did not line up, possibly from the light source not being centered correctly on the sample during one of the data collection periods. Annette Richard provided a diffuse reflectance spectrum for Sn_2S_3 from the fiber optic system that did not have this issue. The NIR data from the split set more closely matches Annette's data than does the UV-Vis, and so we use the NIR data when finding the bandgaps.

Band structure calculations in Wien2k indicated that there should be a difference of approximately 0.3 eV between the bandgap for $SnZrS_3$ and Sn_2S_3 [4]. However, our measurements indicate that the bandgaps are almost identical, differing only by a few hundredths of an eV. One possible explanation of this is that Sn and Zr are chemically very different, because the valence orbitals are p-orbitals for Sn and d-orbitals for Zr.

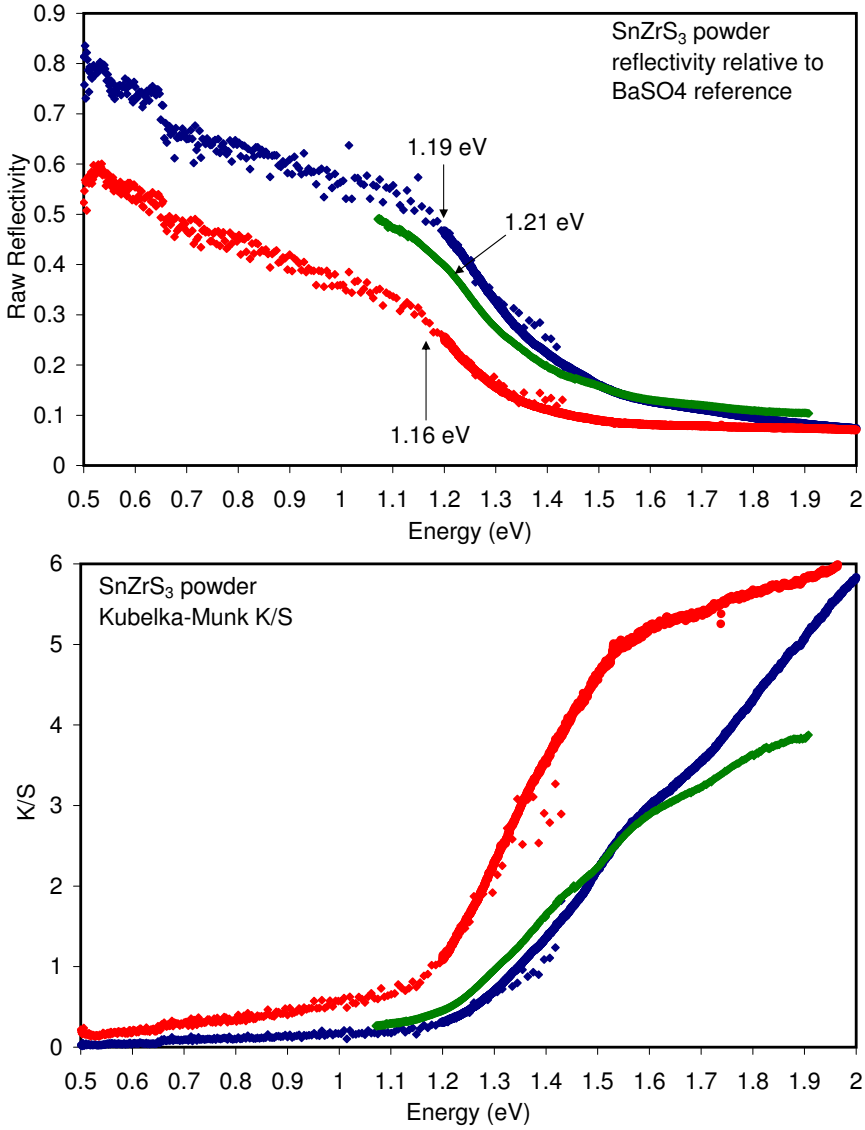

FIGURE 3.11: $SnZrS_3$ diffuse reflectivity (top) and K/S (bottom) plots. The blue and red data sets are from two different samples on the fiber optic system. The green data is the same sample as the blue set, but using the integrating sphere setup with a Si detector. Bandgaps as found via [28] are indicated on the reflectivity plot.

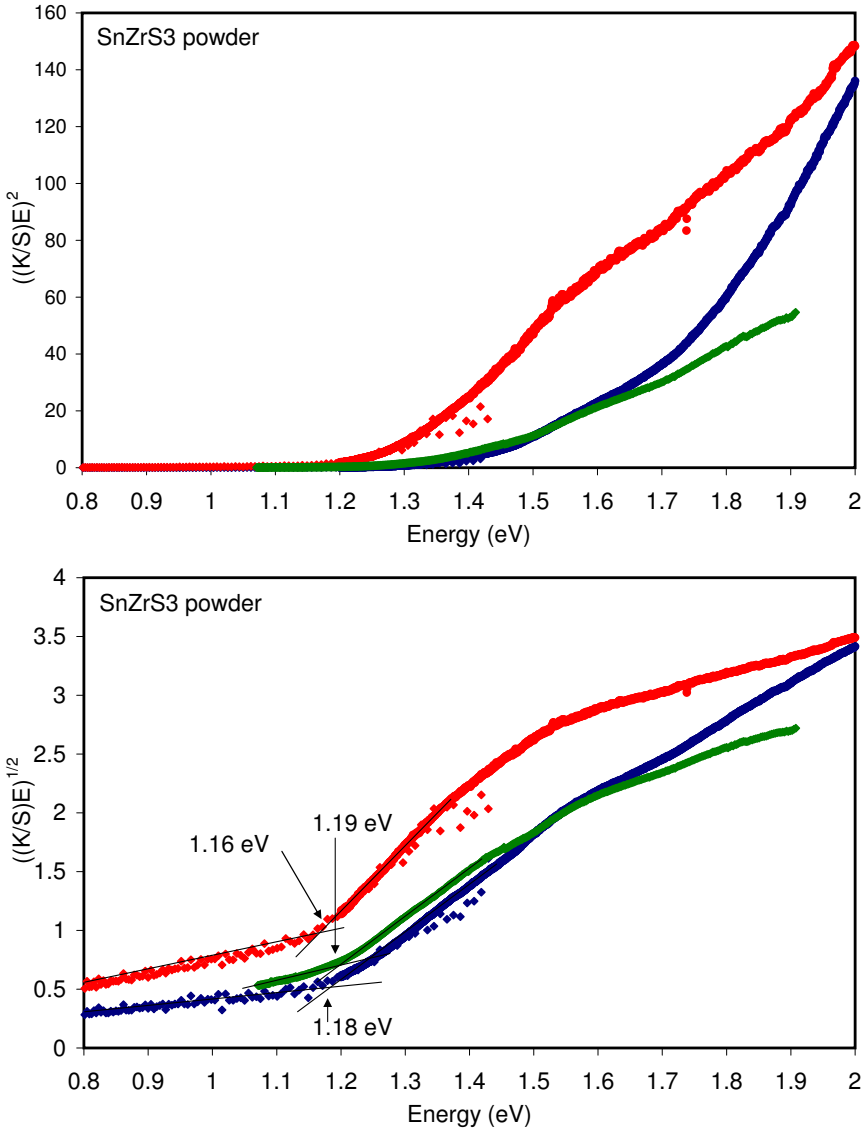

FIGURE 3.12: $SnZrS_3$ $((K/S)E)^2$ (top) and $((K/S)E)^{1/2}$ (bottom) vs. energy plots. The blue and red data sets are from two different samples on the fiber optic system. The green data is the same sample as the blue set, but using the integrating sphere setup with a Si detector. Since $SnZrS_3$ is calculated to have an indirect bandgap, we use the $((K/S)E)^{1/2}$ plot to determine the bandgap. Extrapolating the linear region down to the baseline $((K/S)E)^{1/2}$ value gives bandgaps of 1.16 eV to 1.19 eV.

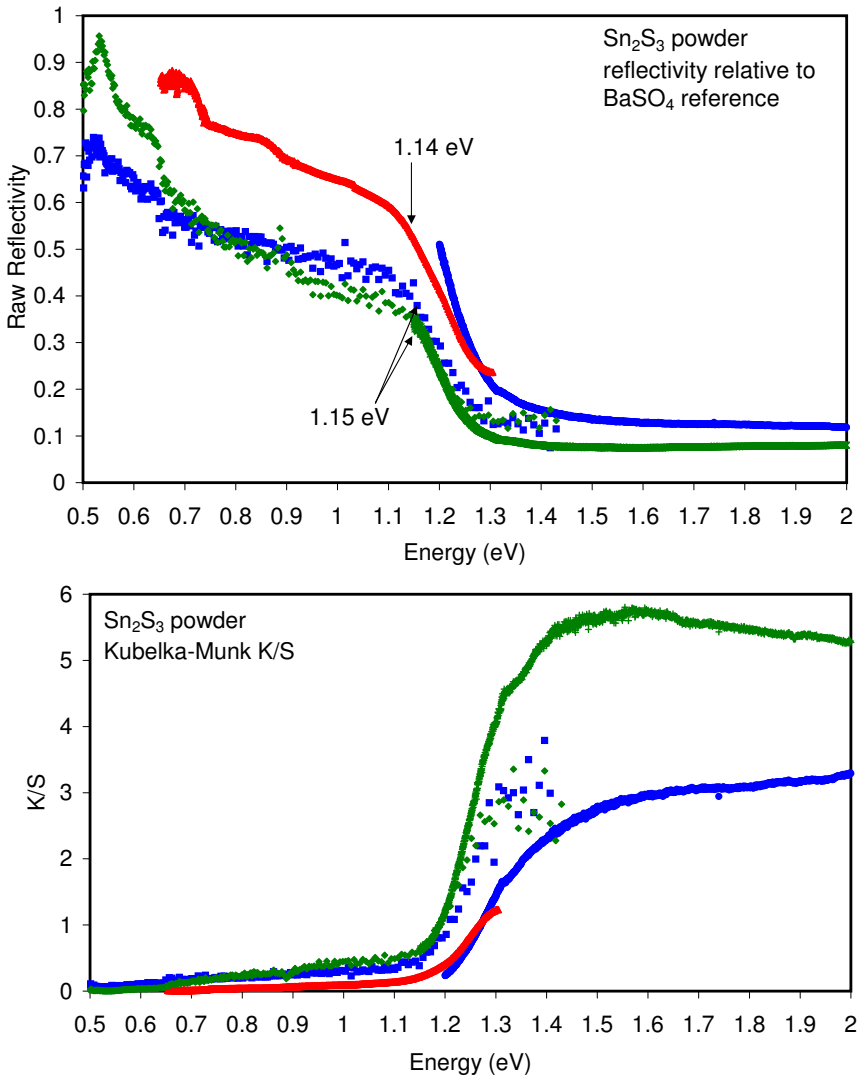

FIGURE 3.13: Sn_2S_3 diffuse reflectivity (top) and K/S (bottom) plots. The red data set is from the integrating sphere setup with an InGaAs detector. The blue and green data sets are two different samples measured on the fiber optics system. The green data set was provided by Annette Richard. Bandgaps as found via [28] are indicated in the reflectivity plot.

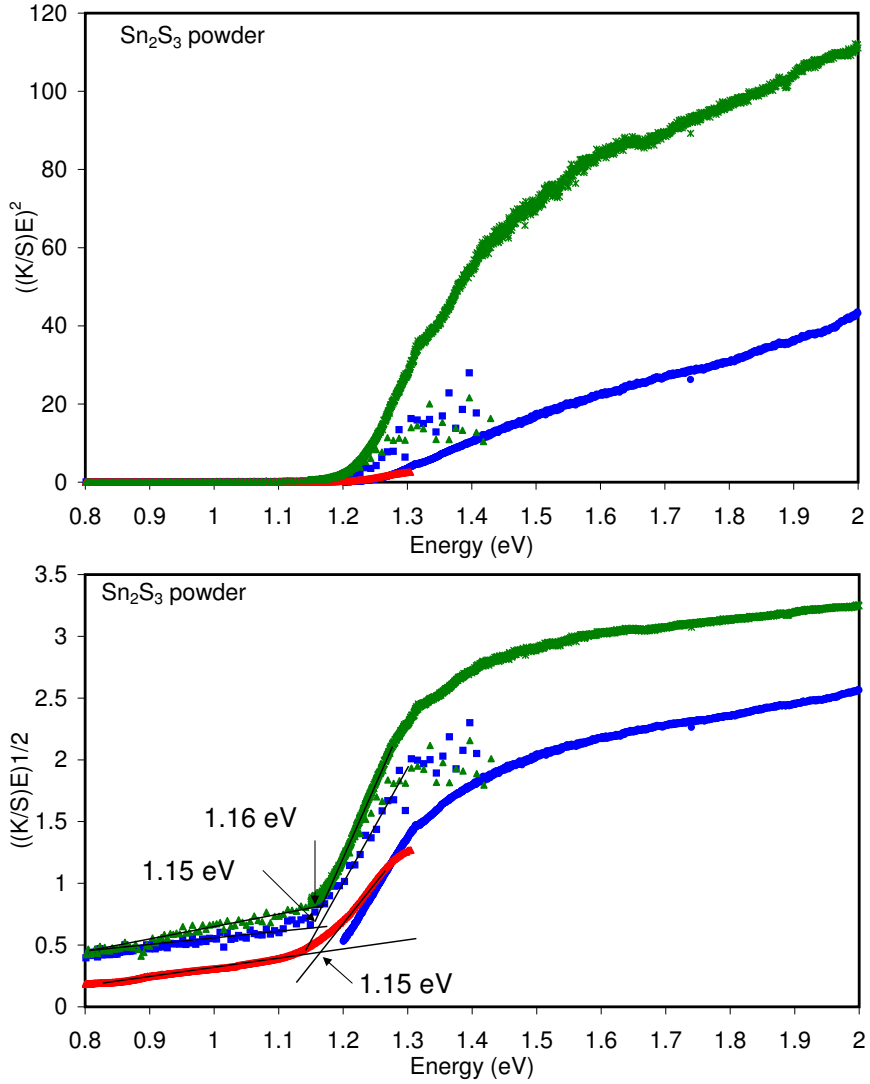

FIGURE 3.14: Sn_2S_3 $((K/S)E)^2$ (top) and $((K/S)E)^{1/2}$ (bottom) vs. energy plots. The red data set is from the integrating sphere setup with an InGaAs detector. The blue and green data sets are two different samples measured on the fiber optics system. The green data set was provided by Annette Richard. Extrapolating the linear region of the $((K/S)E)^{1/2}$ plot down to the baseline value gives bandgaps of 1.15 eV to 1.16 eV.

Bandgap trends from DFT calculations may not hold as we would expect them to when substituting similar elements, such as in $SnZrS_3$ and $SnZrSe_3$.

3.2.4 $SnZrS_3$-Sn_2S_3 Solid Solution

Due to the similar composition and lattice parameters between $SnZrS_3$ ($a = 9.188$ Å, $b = 3.717$ Å, $c = 13.839$ Å) and Sn_2S_3 ($a = 8.878$ Å, $b = 3.751$ Å, $c = 14.020$ Å), it was believed that a solid solution between these two materials could be obtained. If these materials were fully soluble, then material properties such as the bandgap and resistivity could be tuned by substituting appropriate amounts of Sn for Zr. Elemental powders were mixed with the stoichiometry of $Sn_{2-x}Zr_xS_3$, with x ranging from 0 to 1 in increments of 0.1. For $x = 0$ the samples were sintered at 650 °C, 0.1 and 0.2 at 675 °C, 0.3 and 0.4 at 700 °C, 0.5 and 0.6 at 725 °C, 0.7 and 0.8 at 750 °C, and 0.9 and 1.0 at 775 °C.

If a solid solution forms, we expect there to be a smooth transition in XRD peak locations as Sn is substituted for Zr. Figure 3.15 shows the XRD patterns for the $Sn_{2-x}Zr_xS_3$ samples. It can be seen from these patterns that there is not a smooth transition of peaks between $SnZrS_3$ and Sn_2S_3. Instead, we see that from $x = 0.2$ to 0.7, there is the presence of peaks from both $SnZrS_3$ and Sn_2S_3, which would indicate a mixture rather than a solid solution. We also have the presence of SnS_2 in the Sn rich samples, which scales with the amount of Sn. One possible reason for this is that SnS_2 takes a very long time to form, whereas $SnZrS_3$ forms very quickly. It is possible that sinter times in excess of 100 hours as those in [5] would yield a solution.

3.2.5 Doping

Attempts at doping in the $SnZrS_3$ system have been made, but without consistent results. Doping was attempted early on in the project when we had not yet determined the most appropriate synthesis conditions, and so the doped samples were also prone to impurity phases which affected the results.

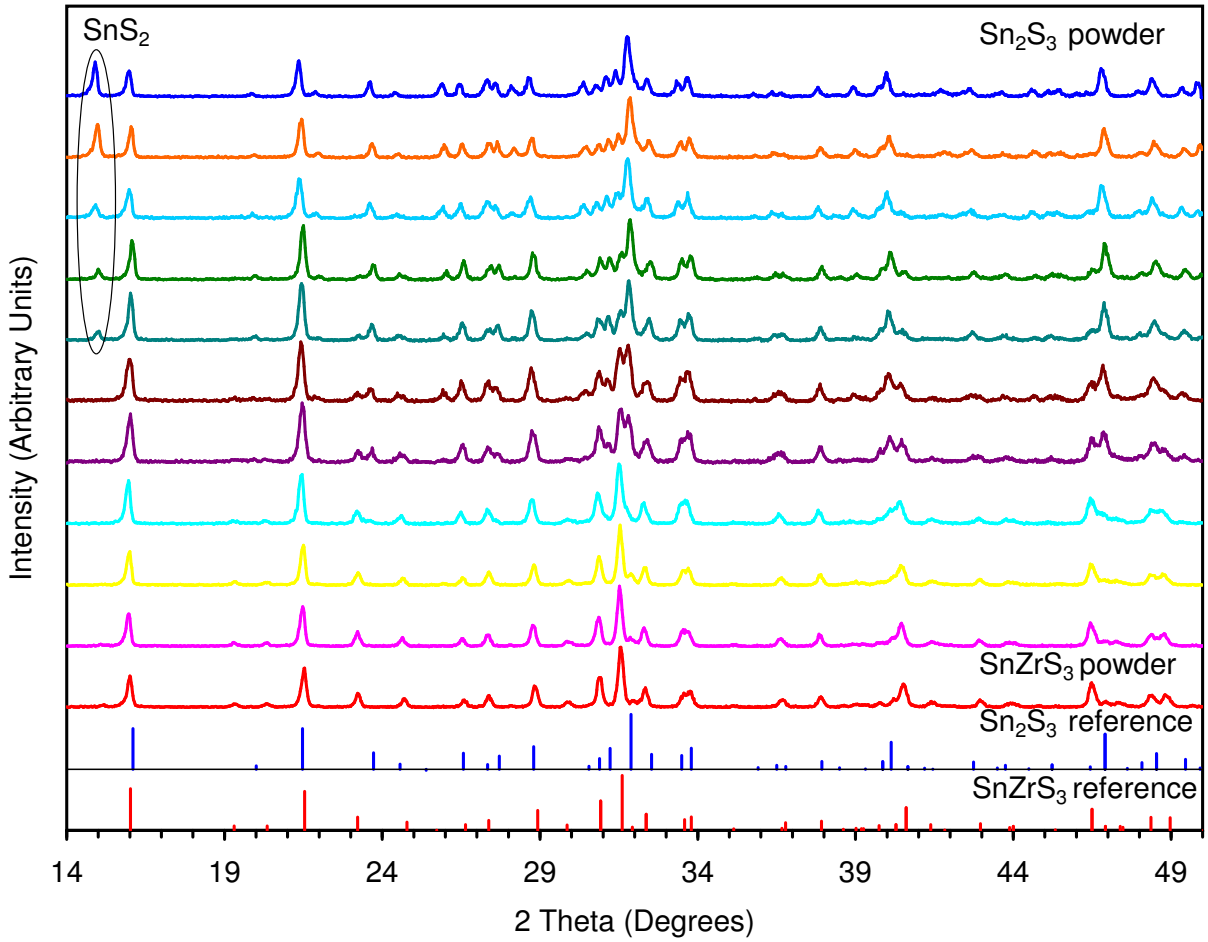

FIGURE 3.15: $SnZrS_3$-Sn_2S_3 solid solution XRD patterns. The bottom pattern (red) reference pattern is for $SnZrS_3$, from [1]. The top (blue) reference pattern is for Sn_2S_3, from [41]. The measured patterns are for $Sn_{2-x}Zr_xS_3$, with the bottom (red) pattern for $x = 1$ ($SnZrS_3$), the top (blue) for $x = 0$ (Sn_2S_3), and the patterns in between are in increments of $x = 0.1$. As the Sn content is increased we see an SnS_2 impurity forming, whose main peak lies at 15°. The doublets of peaks that form at 31-32°, 40°, and 47° indicate that a mixture forms, rather than a solid solution.

Replacing 5, 10, or 15 % of the Zr with In produced a powder which was too resistive to measure the Seebeck coefficient. Bi doping on the Sn site have given samples with positive Seebeck coefficients. However, Bi doping in the selenide system ($SnZrSe_3$) has produced negative Seebeck coefficients.

Doping with 10 % Sb on the Sn site consistenly produced p-type conductivity, with a Seebeck coefficient which ranged from $+170\mu V/K$ to $+2200\mu V/K$. Previous work had shown Sb to be an n-type dopant, however, there were large ZrS_2 impurity phases in those samples. Doping with Sb in $SnZrSe_3$ has produced both n- and p-type conductivity.

4. CONCLUSIONS AND FUTURE WORK

A method for making phase pure $SnZrS_3$ has been found. Solid state reaction of the elements at 800 °C for 12 hours in the stoichiometry $SnZrS_{3/05}$ will consistently make phase pure powder. A suitable method has not yet been found for phase pure synthesis of Sn_2S_3. Solid state reaction of the elements at 650 to 750 °C for 12 hours will yield Sn_2S_3 and a small amount of SnS. The complete solid solution of $SnZrS_3$ and Sn_2S_3 does not seem to form, though replacing up to 20% of the Zr with Sn does not noticeable Sn_2S_3 peaks or impurity phases. At 10% Zr for Sn there are no detectable traces of $SnZrS_3$, but at 20% we begin to see shoulders where $SnZrS_3$ peaks will form. Table 4.1 summarizes the optical and transport results for $SnZrS_3$ and Sn_2S_3.

Material	E_g	Seebeck coefficient	Resistivity
$SnZrS_3$	1.16-1.21 eV	600-700 μV/K	13 MΩcm
Sn_2S_3	1.14-1.16 eV	+1000 μV/K	216 kΩcm

TABLE 4.1: Results summary

If Sn_2S_3 phase purity is desired, longer sinter times are likely to be necessary. Raising the synthesis temperature from 650 °C to 750 °C may help quicken the reaction. If phase purity is achieved through increased sinter temperatures and times, then perhaps the $SnZrS_3$-Sn_2S_3 solid solution will also benefit from the same growth modifications.

Further work is required to make conclusive statements about doping in the $SnZrS_3$ system. In view of Zunger's doping rules [24], investigations into electron affinities and ionization energies may be useful for this system, and for any future system we wish to dope. In materials which form solid solutions, conduction band minima and valence band maxima could possibly be shifted by varying the solution composition, which will change the electron affinity or ionization energy. While the $SnZrS_3$-Sn_2S_3 might not be a viable

option for such band structure modification, there are other possible solutions to be made. Hf could replace Zr with no change in valence. Ti is another possibility for an isovalent dopant on the Zr site. Ge and Pb could be put in the Sn site, and Se and Te could be used on the S site. Band structure calculations for each of these materials could be utilized to determine if these replacements might change the structure enough to significantly change the electron affinity or ionization energy.

Since all of our doping efforts to date have been on the cation sites, the synthesis of $SnZrS_3$ with excess S appears to have the potential to make doping efforts more fruitful, due to creating an anion rich synthesis environment. Doping with In currently does not seem to be a productive route, but is perhaps worth revisiting under anion rich conditions. There has been some success with using Nb as an *n*-type dopant in the $SnZrSe_3$ system, perhaps similar success will be found in the sulfide system. A possible *p*-type dopant is Y.

BIBLIOGRAPHY

1. A. Meetsma, G. Wiegers, and J. de Boer, "Structure determination of $SnZrS_3$," *Acta Crystallographica Section C*, vol. 49, pp. 2060–2062, 1993.

2. R. Kniep, D. Mootz, U. Severin, and H. Wunderlich, "Structure of Tin(II)Tin(IV)Trisulphide, a redetermination," *Acta Crystallagraphica B*, vol. 38, pp. 2022–2023, 1982.

3. U. Alpen, J. Fenner, and E. Gmelin, "Semiconductors of the type $Me^{II}Me^{IV}S_3$," *Materials Research Bulletin*, vol. 10, pp. 175–180, 1975.

4. A. Richard, J. Russel, D. Harada, A. Zakutayev, J. Francis, R. Kykyneshi, J. Tate, D. Keszler, G. Schneider, and A. Klein, "Band structure investigations of $SnMCh_3$ (M=Sn, Zr, and Hf; Ch= S and Se)." article pre-print.

5. G. Moh, "The tin-sulfur system and related minerals," *Neues Jahrbuch fur Mineralogie. Abhandlungen*, vol. 111, pp. 227–263, 1969.

6. P. Harrison, ed., *Chemistry of Tin*. Chapman and Hall, 1989.

7. S. del Buchia, J. Jumas, and M. Maurin, "Contribution l'tude de composs sulfurs d'tain(ii): affinement de la structure de SnS," *Acta Crystallographica Section B*, vol. 37, pp. 1903–1905, 1981.

8. S. Cheng, Y. Chen, Y. He, and G. Chen, "The structure and properties of SnS thin films prepared by pulse electro-deposition," *Materials Letters*, vol. 61, pp. 1408–1412, 2007.

9. R. Miles, O. Ogah, G. Zoppi, and I. Forbes, "Thermally evaporated thin films of SnS for applications in solar cell devices," *Thin Solid Films*, vol. 517, pp. 4702–4705, 2009.

10. B. Ghosh, M. Das, P. Banerjee, and S. Das, "Fabrication and optical properties of SnS thin films by SILAR method," *Materials Letters*, vol. 61, pp. 1408–1412, 2007.

11. Z. Zainal, M. Hussein, and A. Ghazali, "Cathodic electrodeposition of SnS thin films from aqueous solution," *Solar Energy Materials and Solar Cells*, vol. 40, pp. 347–357, 1996.

12. F. Gashimzade, D. Guliev, D. Guseinova, and V. Shteinshrayber, "Band-structure calculation for A^4B^6 layered crystals by the equivalent-orbital linear combination of atomic orbitals method," *Journal of Physics: Condensed Matter*, vol. 4, pp. 1081–1091, 1992.

13. J. Anderson and M. Morton, "The electrical conductivity of stannous sulphide," *Proceedings of the Royal Society of London Series A*, vol. 184, pp. 83–101, 1944.

14. B. Palosz and E. Salje, "Lattice parameters and spontaneous strain in ax_2 polytypes: CdI_2, PbI_2, SnS_2 and $SnSe_2$," *Journal of Applied Crystallography*, vol. 22, pp. 622–623, 1989.

15. N. Deshpande, A. Sagade, Y. Gudage, C. Lokhande, and R. Sharma, "Growth and characterization of tin disulfide (SnS_2) thin film deposited by successive ionic layer adsorption and reaction (SILAR) technique," *Journal of Alloys and Compounds*, vol. 436, pp. 421–426, 2007.

16. A. Sanchez-Juarez, A. Tirbucio-Silver, and A. Ortiz, "Fabrication of SnS_2/SnS heterojunction thin film diodes by plasma-enhanced chemical vapor deposition," *Thin Solid Films*, vol. 480-481, pp. 452–456, 2005.

17. M. Botero, C. Cifuentes, E. Romero, J. Clavijo, and G. Gordillo, "Properties of SnS thin films grown by a two-step process," in *Conference record of the 2006 IEEE 4th world conference on Photovoltaic energy conversion*, pp. 79–82, 2006.

18. D. Greenaway and R. Nitsche, "Preparation and optical properties of group $IVVI_2$ chalcogenides having the CdI_2 structure," *Journal of Physics and Chemistry of Solids*, vol. 26, pp. 1445–1458, 1965.

19. A. Clearfield, "The synthesis and properties of zirconium disulfide," *Journal of the American Chemical Society*, vol. 80, pp. 6511–6513, 1958.

20. M. Moustafa, T. Zandt, C. Janowitz, and R. Manzke, "Growth and band gap determination of the ZrS_xSe_{2-x} single crystal series," *Physical Review B*, vol. 80, p. 035206, 2009.

21. S. Srivastava and B. Avasthi, "Preparation, structure and properties of transition metal trichalcogenides," *Journal of Materials Science*, vol. 27, pp. 3693–3705, 1992.

22. S. Patel, S. Chaki, and A. Agarwal, "Growth and electrical properties of zirconium trisulphide single crystals," *Physica Status Solidi (a)*, vol. 140, pp. 207–212, 1993.

23. S. Furuseth, L. Brattas, and A. Kjekshus, "Crystal structures of TiS_3, ZrS_3, $ZrSe_3$, $ZrTe_3$, HfS_3, and $HfSe_3$," *Acta Chemica Scandinavica*, vol. 29, p. 623, 1975.

24. A. Zunger, "Practical doping principles," *Applied Physics Letters*, vol. 83, pp. 53–59, 2003.

25. D. Cohen, "Earth's natural wealth: an audit," *NewScientist*, 2007.

26. G. Will, *Powder Diffraction: The Rietveld Method and the Two-Stage method*. Springer, 2006.

27. L. Aslanov, F. G., and A. Howard, *Crystallographic Instrumnentation.* Oxford University Press, 1998.

28. P. Fochs, "The measurement of the energy gap of semiconductors from their diffuse reflectance spectra," *Procedings of the Physical Society Section B*, vol. 69, pp. 70–75, 1956.

29. P. Yu and M. Cardona, *Fundamentals of Semiconductors.* Springer, 2001.

30. R. Smith, *Wave Mechanics of Crystalline Solids.* Chapman and Hall LTD, 1969.

31. J. Hodgson, *Optical Absorption and Dispersion in Solids.* Chapman and Hall LTD, 1970.

32. A. Christy, O. Kvalheim, and R. Velapoldi, "Quantative analysis in diffuse reflectance spectrometry: A modified Kubelka-Munk equation," *Vibrational Spectroscopy*, vol. 9, pp. 19–27, 1995.

33. L. Yang and B. Kruse, "Revised Kubelka-Munk theory. I. Theory and application.," *Journal of the Optical Society of America A*, vol. 21, pp. 1933–1941, 2004.

34. D. MacDonald, *Thermoelectricity: an introduction to the principles.* John Wiley & Sons, 1962.

35. D. Schroder, *Semiconductor material and device characterization.* Wiley-Interscience, Third ed., 2006.

36. K. Seeger, *Semiconductor Physics: an introduction.* Springer-Verlag, 1982.

37. L. Van der Pauw, "A method of measuring specific resistivity and Hall effect of discs of arbitrary shape," *Philips Research Reports*, vol. 13, pp. 1–9, 1958.

38. D. Look, *Electrical characterization of GaAs materials and devices.* John Wiley & Sons, 1989.

39. R. Rice, "Evaluation and extension of physical property-porosity models based on minimum solid area," *Journal of Materials Science*, vol. 31, pp. 102–118, 1996.

40. A. van Arkel, "The tin-sulfur system and related minerals," *Physica B+C*, vol. 4, p. 286, 1924.

41. M. Cruz, J. Morales, J. Espinos, and J. Sanz, "XRD, XPS and ^{119}Sn NMR study of tin sulfides obtained by using chemical vapor transport methods," *Journal of Solid State Chemistry*, vol. 175, pp. 359–365, 2003.